MASTER OF SCIENCE (2009) McMaster University

(Department of Physics and Astronomy) Hamilton, Ontario

TITLE: Properties of Galaxy Dark Matter Halos using galaxy-galaxy weak lensing in the CFHTLS-Deep

AUTHOR: Jennifer Golding, HB.Sc.

SUPERVISOR: Laura C. Parker

NUMBER OF PAGES: 10, ??

Properties of Galaxy Dark Matter Halos using galaxy-galaxy weak lensing in the CFHTLS-Deep

By

Jennifer A. Golding, HB.Sc.

A Thesis

Submitted to the School of Graduate Studies

in Partial Fulfilment of the Requirements

for the Degree

Master of Science

McMaster University

Properties of Galaxy Dark Matter Halos

Abstract

Gravitational lensing can be used as a direct probe of the distribution of dark matter around galaxies, groups, and clusters, making it a powerful tool in astrophysics. In this thesis, we introduce the basics of gravitational lensing and weak gravitational lensing. Using weak lensing to study the ensemble-averaged properties of a population of objects, we present a study of galaxy-galaxy lensing of galaxy-sized dark matter halos using data from the Canada-France-Hawaii Telescope Legacy Survey (CFHTLS) Deep.

We calculated the average velocity dispersion for an L_* galaxy at a redshift of 0.54 to be 113 ± 9 kms^{-1}, with a mass of 1.7 ± 0.3 x 10^{12} h^{-1}M$_\odot$. We present the first conclusive evidence for non-spherical galaxy dark matter halos. Our results favour a dark matter halo with an ellipticity of 0.70 ± 0.18 at $> 5\sigma$ when averaged over all galaxies. If the sample of foreground lens galaxies is selected by colour, we detect non-spherical halos for all 4 samples except a green subsample. We also consider samples of galaxies divided by colour, redshift and luminosity. Our luminosity samples allowed us to calculate a B-band Tully-Fisher relation which is consistent with theoretical predictions. From our data, we do not detect any evolution in galaxy dark matter halos from a redshift of 0.78 to 0.39, corresponding to no evolution from when the Universe was 6.6 Gyr to 9.1 Gyr old in a ΛCDM cosmology.

Acknowledgements

I would like to acknowledge my supervisor Dr. Laura Parker. Her guidance, continuous support, and endless patience made this project enjoyable and possible.

I would like to thank my Master's committee members Dr. Doug Welch and Dr. Christine Wilson, for their helpful comments, and suggestions pertaining to this project.

It is necessary to thank the following graduate students, without whom, I would have either not finished this degree, or would have lost my mind while trying: Kristin Woodley, Juan Madrid, Robbie Henderson, and Tara Parkin.

Finally, I would like to thank my family, and friends for their love, support, and complete confidence in me over the last two years. Without your help and support this would not have been possible.

To my wonderful daughter Alyssa, you helped to make this all worth it. Thank you.

Table of Contents

List of Figures

List of Tables

Chapter 1

Introduction

It has been 400 years since Galileo Galilei first pointed a telescope to the skies in the interest of learning more about the Universe. In this time, much has been learned about stars, planets, galaxies, and even larger structures in the Universe. We have learned that we live on a planet that is evolving and orbiting around a star we call the Sun, and that both reside in one spiral arm of a massive galaxy called the Milky Way. In the past 400 years we have also learned that our galaxy is only one of many billions in an amazing and expanding Universe.

While there is much that has been learned through both observations and theory, there is still much that is unknown or poorly understood. In the past 100 years we have learned that the Universe is mostly made up of matter that cannot be seen, and that this matter makes up over 90% of the mass in our own galaxy. This mysterious matter, known as "dark matter" permeates the entire Universe, and even now, its nature remains elusive. What is known is that it plays an important role in structure formation, and plays a role in how galaxies form and evolve over time. Understanding more about dark matter will allow us to understand more about how galaxies formed in the early Universe, and how they have evolved into the galaxies we see today.

This thesis will introduce the topics of galaxies and dark matter and then discuss how dark matter can be detected and studied in galaxies using weak gravitational lensing.

1.1 Galaxies

A galaxy is a massive system bound by gravity that consists of stars, gas, dust, and a poorly understood but important component known as dark matter. Currently, we know that galaxies come in different sizes (dwarfs to giants) and shapes, (e.g. elliptical, irregular, and spiral) and contain anywhere from $\sim 10^7$ to 10^{12} stars. What we do not know in detail, is how galaxies have formed, their evolutionary history, and what role dark matter plays in their formation and evolution.

Historically, theories of galaxy formation were divided into two categories: top-down and bottom-up. In top-down theories such as the EggenLynden-BellSandage [ELS] model (Eggen, Lynden-Bell & Sandage, 1962), primordial galaxies form in a large-scale simultaneous collapse lasting about one hundred million years . In bottom-up theories (Peebles, 1968; Press & Schechter, 1974), small structures such as globular clusters and dwarf galaxies form first, and then a number of such bodies accrete to form galaxies and clusters. More recent theories include the clustering of dark matter halos in the bottom-up process (White & Frenk, 1991; Fukushige & Makino, 1997). All evidence to date points to the bottom-up approach as large structures such as clusters of galaxies are much more prevalent at z = 0 than at higher redshifts.

1.2 Dark Matter

Dark matter is matter that cannot be detected by the standard means as it neither emits nor absorbs electromagnetic radiation. Instead its presence is inferred from its gravitational effects on visible matter by observing the radial velocities of stars in galaxies. This mysterious material has been postulated to explain many observed phemomena such as the flat rotation curves of spiral galaxies (Rubin & Ford, 1970) and the unexpectedly high orbital velocities of galaxies in clusters (Zwicky, 1933). According to observations, dark matter and another mysterious component in the Universe, dark energy (which will not be discussed in detail), account for the vast majority of the energy density in the observable Universe.

1.2.1 Evidence for the existence of Dark Matter

While we have learned that dark matter is not made up of black holes or brown dwarfs (for example), we still do not know exactly what dark matter is. It plays a significant role in structure formation and galaxy evolution (Combes, 2004), and has measurable effects on cosmic microwave background anisotropies (Komatsu et al., 2009). All lines of evidence suggest that galaxies, groups of galaxies, clusters of galaxies and the Universe as a whole, contain much more matter than is seen. 5-year measurements from the Wilkinson Microwave Anisotropy Probe (WMAP) (Komatsu et al., 2009) have been interpreted to mean the Universe has a dark matter component that comprises 21.4% of the mass in the Universe, whereas baryonic material only makes up 4.4%.

One of the most solid pieces of evidence for the existence of dark matter came from studies of galaxy rotation curves. Vera Rubin and her collaborators in the 1970's first noted that spiral galaxy rotation curves were flat (Rubin & Ford, 1970), meaning that stars in the outer parts of the galaxy were orbiting at roughly the same speed as those found in the inner regions (see Figure 1.1). This result implied that there was more mass in the outer regions of galaxies than could be accounted for by gas and stars.

Recently, a galaxy named VIRGOHI 21 (in the Virgo Cluster) was observed (Minchin et al., 2005; 2007), and no visible stars were detected. Based on rotation profiles of the galaxy, VIRGOHI 21 is estimated to contain $\sim$ 1000 times more dark matter than hydrogen and has a total mass $\sim$ 1/10 of the Milky Way. VIRGOHI 21 has been dubbed a "Dark Galaxy", and if its existence is confirmed, as others have suggested that VIRGOHI 21 is just tidal debris from a nearby galaxy (Duc, Bournaud & Brinks, 2008), it has significant implications in galaxy structure and formation theories and for alternative explanations for dark matter such as Modified Newtonian Dynamics (MOND) (Milgrom, 2002).

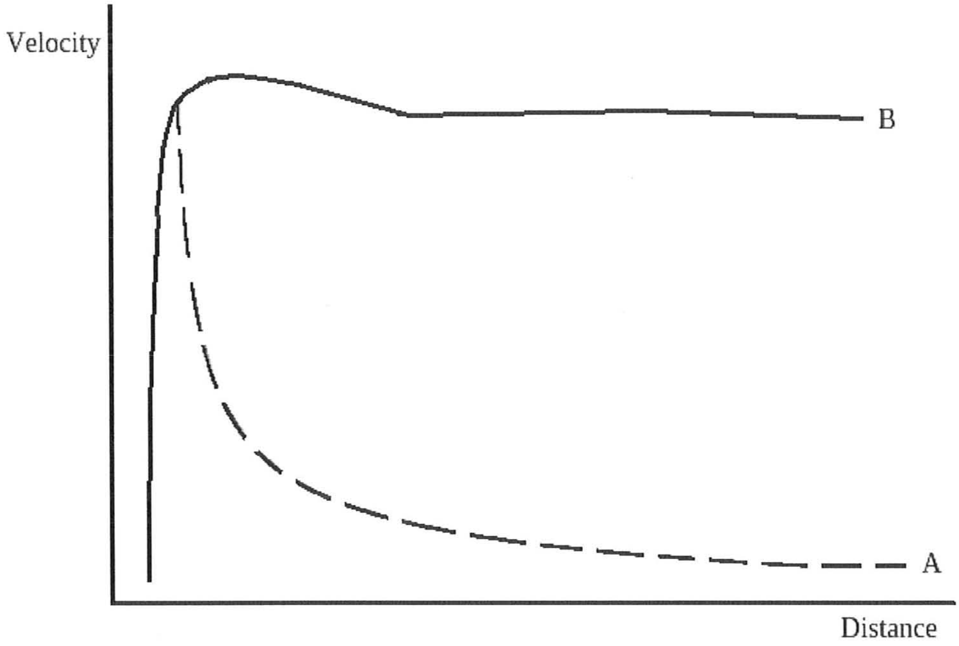

Figure 1.1 : Schematic of a disk galaxy rotation curve. The dashed line is the rotation curve expected for an object in a Keplerian orbit. The solid line is what is typically observed. Adding a smooth dark matter component with a density profile of $\rho \propto \mathrm{r}^{-2}$ to the expected results, fits most observations quite well.

While today bottom-up structure formation theory is widely accepted in a Λ Cold Dark Matter (CDM) cosmology (Riess et al., 1998; Perlmutter et al., 1999; Komatsu et al., 2009), there is still much to be understood about just how the dark matter is distributed in galaxies, if it is a function of galaxy type, as dwarf galaxies appear to contain the most dark matter (Penny et al., 2009), and how the content changes as galaxies evolve and merge together. This is a question that one can try to answer through the use of gravitational lensing.

Gravitational lensing can be used as a direct probe of the total mass, and thus the total dark matter content of a galaxy. Using weak gravitational lensing specifically, one can probe the dark matter content of individual galaxies out to great distances, and learn more about the properties of dark matter on galaxy scales. This will be discussed in more detail in section 1.3.

1.2.2 What is Dark Matter?

While no one has yet managed to determine exactly what dark matter is, there are some theories as to what it could be. Currently, the majority of dark matter is believed to be non-baryonic, meaning it is not made up of baryonic matter (normal matter made of protons and neutrons) and it does not interact with ordinary matter electromagnetically. The baryonic form of dark matter, which comprises a very small fraction of the total dark matter content in the Universe, is believed to be in the form of non-luminous gas, brown dwarfs, and Massive Astrophysical Compact Halo Objects (MACHOs) (see Alcock et al., 2000; Tisserand et al., 2007). The non-baryonic component of dark matter may consist of multiple particles, including a small fraction of neutrinos which have been shown to have mass (e.g. Fukuda et al., 1998), and hypothetical particles such as axions or supersymmetric particles.

Understanding the nature of dark matter is very important in astrophysics, but also in other fields such as particle physics and quantum gravity. While no conclusive results exist to date, there are some prospects for directly detecting dark matter particles with massive particle detectors (e.g. Angloher et al., 2009).

1.3 Gravitational Lensing

A gravitational lens is formed when the light from a background source (such as a quasar) appears to be bent around a massive object (such as a group of galaxies) between the source object and the observer (light always travels in straight lines). The process is known as gravitational lensing, and is one of the predictions of Albert Einstein's general theory of relativity. The gravity from a massive object (such as a galaxy or galaxy cluster) curves space-time, and alters the apparent paths followed by light rays from a background source. This can both magnify and distort the apparent image of the background source.

1.3.1 Background in Lensing

The gravitational lensing signal that one can detect is determined by the mass of the lens and the overall geometry of the system. Unlike with an optical lens, the minimum apparent 'bending' occurs furthest from, and the maximum apparent 'bending' occurs closest to the centre of a gravitational lens (see Figure 1.2). Thus, if the alignment along the line of sight is close between the observer, lens and source, the lensing signal is stronger than if the alignment is not close (see Figure 1.3). Gravitational lensing can generally be divided into 2 categories:

1) **Strong lensing**: where the distortions are easily visible, such as the formation of multiple images and arcs (see Figure 1.4). A subclass of strong lensing is microlensing, where unresolved multiple images are seen and there is a brightening in the light from the source, which has a characteristic light curve. The background source and the lens in a typical case are stars in our own galaxy, the Milky Way.

2) **Weak lensing**: the distortions of background sources by foreground lenses are very small (due to intrinsic ellipticities) and can only be detected statistically by analysing a large number of sources to find coherent distortions of the order of a few percent. Lenses can be individual galaxies, groups of galaxies, galaxy clusters, or even the large scale structure of the Universe. The lensing signal is seen as a preferential stretching of the background objects tangential to the lensing object.

We will now give a brief discussion of some of the equations used in lensing and then discuss weak lensing in more detail, and the applications of gravitational lensing, with a focus on weak lensing. For a more detailed review on the lensing equations, see Mellier (1999) or Bartelmann & Schneider (2001).

The bending of light around a mass, M, is given by

$$\alpha = \frac{4GM}{bc^2}, \tag{1.1}$$

where c is the speed of light, b is the impact parameter of the light ray, and G is the gravitational constant as seen in Figure 1.3. If the observer, lens, and source are aligned exactly, then the image of the source will be in the form of a circle (if the source is a point source), where the radius is called the *Einstein radius*, θ_E, and is described by

$$\theta_E = \left(\frac{4GM}{c^2}\frac{D_{LS}}{D_L D_S}\right)^{1/2}, \tag{1.2}$$

where D_L is the angular diameter distance to the lens, D_S the angular diameter distance to the source, and D_{LS} the angular diameter distance between the lens and source. One popular lens model, and the one utilized in this work, is the isothermal sphere model. This mass distribution has a density profile $\rho \propto r^{-2}$, and appears to fit most observations quite well, as well as being roughly consistent with results from numerical simulations over the range of interest (Klypin, 2000). The mass distribution from the isothermal sphere model, yields an Einstein radius of

$$\theta_E = \left(\frac{4\pi\sigma^2}{c^2}\right)\frac{D_{LS}}{D_S} \text{ radians} \tag{1.3}$$

rescaled this gives

$$\theta_E = \left(\frac{\sigma}{186kms^{-1}}\right)^2 \beta[''], \tag{1.4}$$

where

$$\beta = \left[\frac{D_{LS}}{D_S}\right], \tag{1.5}$$

and σ is the line of sight velocity dispersion of the lens.

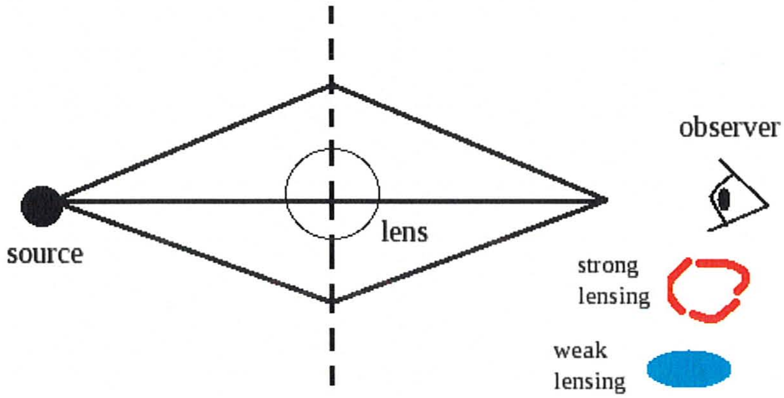

Figure 1.2 : Strong and weak lensing regimes. When the alignment between the source, lens and observer is poor, distant sources are slightly distorted and are known as arclets. When the alignment is close, multiple images and giant arcs can form. See Figure 1.4. The weak distortion found with poor alignment must be measured statistically through a method called weak graviational lensing.

1.3.2 Weak Lensing

Weak lensing is statistical in nature. Using shapes of background sources which have large instrinsic variations in their shapes requires one to measure the shapes of many background galaxies. Individual galaxies and groups of galaxies are not very massive and do not cover large areas of the sky, so the weak lensing signal from multiple systems must be stacked together. By stacking the signal, we can only learn information about the ensemble averaged properties of these systems. Clusters of galaxies on the other hand, are very massive and big on the sky so that there is a significant weak lensing signal and many background sources, and therefore one can measure the properties of

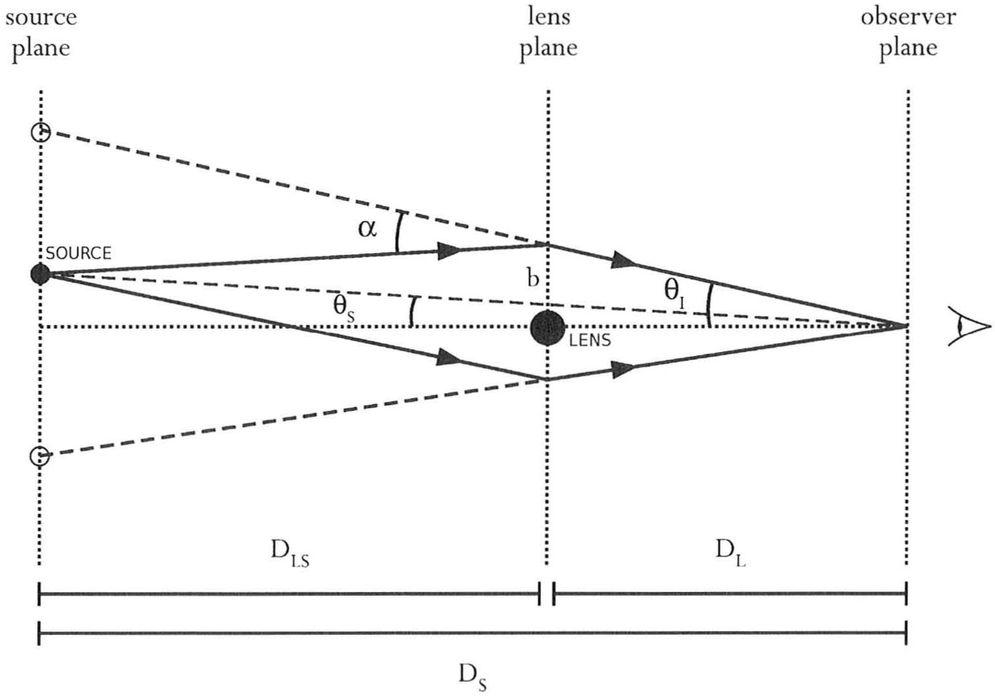

Figure 1.3 : The geometry of a lensing system where D_L, D_S and D_{LS} are the angular diameter distance to the lens, source and between the lens and source respectively. θ_I is the observed angular position of the source, θ_S is the intrinsic position of the source, α is the bending angle, and b is the impact parameter.

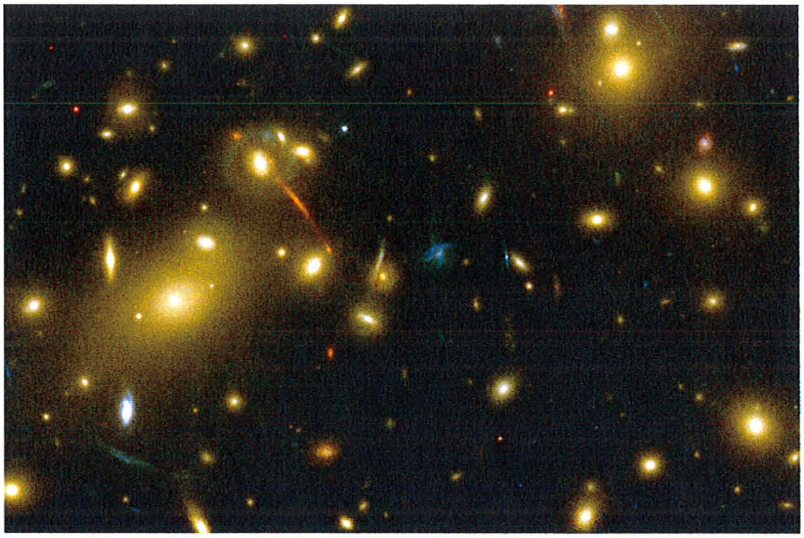

Figure 1.4 : Abell 2218. Multiple strong lensing features are visible in this HST image. Strong lensing arcs are more readily located in space-based observations due to increased spatial resolution. Credit: NASA, Andrew Fruchter and the ERO Team [Sylvia Baggett (STScI), Richard Hook (ST-ECF), Zoltan Levay (STScI)] (STScI)

individual clusters. Weak lensing can be induced by individual galaxies lensing distant background galaxies. This type of weak lensing is known as galaxy-galaxy lensing, and is a way to probe the dark matter distribution on galaxy scales. If the sample of foreground galaxies acting as lenses is large enough, then one can split the lens sample into different redshift, luminosity, or colour bins in order to look for differences in the average dark matter profiles (as will be discussed in Chapter 3). An alternative, but complementary method to learn more about galaxy dark matter halos is using satellite galaxies as tracers of halos (Zaritsky & White, 1994; Prada et al., 2006). This is primarily a low redshift technique, that requires assumptions about the satellite orbits. It is similar to weak lensing in that because there are generally only 2 - 3 satellites detected per galaxy, this technique requires stacking to get a signal.

1.3.3 Lensing Applications

Background Sources

Gravitational lenses can be used as if they were "gravitational telescopes", because they conserve surface brightness, but magnify objects seen behind them, making very faint objects appear brighter and larger and therefore more easily studied. The arcs seen in strong lensing images are very magnified, distant sources which without the magnification from the lensing, would be too faint to study. Some of the highest redshift galaxies (those in early stages of formation) have been found from observing strong lensing clusters (see Zheng et al., 2009).

Foreground Lenses

Observations of gravitational lensing can also be used to examine the lens itself. While most other astronomical observations are sensitive only to emitted light, gravitational lensing is sensitive to the total mass, both luminous and dark. Comparing mass and light generally involves making some assumptions about complicated astrophysical processes. Gravitational lensing is a particularly useful tool for learning more about the lens (galaxy, group, or cluster) because the luminous component of the lens can be observed and the total mass of the system directly inferred.

- **Galaxy Clusters** Using the positions, fluxes and sizes of the arcs found in strong lensing images, one can learn information about the lensing object (Rzepecki et al., 2007). The locations of the arcs are associated with the

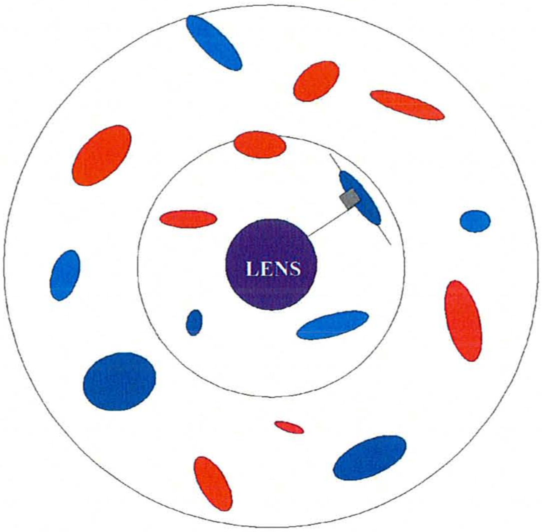

Figure 1.5 : Weak Lensing Schematic. The tangential component of the shapes of background galaxies are calculated around foreground lens objects. The weak lensing signal is this tangential 'shearing', averaged in radial annuli centered on the lens.

Einstein radius of the lens, and are thus useful for studying the mass inside of θ_E.

With weak lensing, individual galaxy clusters are massive enough to be detected and their mass distributions can be measured (Clowe et al., 2006; Umetsu, Takada & Broadhurst, 2007). Weak lensing can be used to reconstruct the cluster mass distribution to distances outside of θ_E, using the fact that every cluster will weakly distort distant galaxies behind it on the sky. Sources will be distorted and show a preferred alignment tangential to the lensing cluster (see schematic in Figure 1.5).

• **Galaxy Groups** The lensing signal induced by galaxy groups is too small to be observed for individual systems and so the signal from multiple groups must be stacked together. Hoekstra et al. (2000) reported the first galaxy group weak lensing measurement, but the significance was low for all groups stacked together. Parker et al. (2005) made a more significant detection of group weak lensing and were able to calculate the radial profile of the M/L ratio. Using data from the Sloan Digital Sky Survey (SDSS), recent galaxy-group weak lensing measurements have been made by Mandelbaum et al. (2006c) and Sheldon et al. (2007).[1]

• **Galaxy-Galaxy Lensing** Understanding the properties of galaxies is an integral part of understanding our Universe as they are some of the earliest structures that formed (Beckwith et al., 2006), and continue to evolve with time. It is only recently that we have begun to understand more about properties such as their masses and sizes. It is well known that galaxies reside in dark matter halos, but there are still a lot of uncertainties about the halo properties. As there are few visible tracers at large radii, rotation curves can only constrain the dark matter content in the inner regions of galaxies. It is important to know more about the dark matter content in galaxies so that we can better understand the dark matter itself, the relationship between dark and luminous matter and how it is involved in the hierarchical growth of galaxies. Gravitational lensing, and specifically weak gravitational lensing, has the ability to trace the distribution of dark matter out to large radii, where other techniques fail and where comparisons to numerical simulations are relevant.

[1] www.sdss.org/

1.3.4 How to Measure Weak Lensing

Ideal surveys for galaxy-galaxy lensing have deep, wide-field data with a redshift for all objects in the field of view. Redshifts are very important for being able to differentiate between foreground and background objects to have a well defined sample of lenses and sources, and for determination of D_L, D_S and D_{LS} (see equation 1.3). Unfortunately, most of the time, the redshifts are unknown. Galaxy-galaxy lensing measurements have been carried out using small areas with spectroscopic redshifts (McKay et al., 2001; Smith et al., 2001; Hoekstra et al., 2003) and wide-fields at low redshifts (Sheldon et al., 2004; Mandelbaum et al., 2006a, 2006b), but generally the redshifts have to be estimated using photometry. If multi-band data are available, then photometric redshifts can be used to estimate the redshifts of the lenses and sources (Hudson et al. 1998; Wilson et al., 2001; Kleinheinrich et al., 2006), but if imaging in one band is all that is available, then some assumptions must be made about the lens and source redshift distributions (Parker et al., 2007). If the lens sample is large enough, it can be divided into sub-samples, segregated by colour, redshift or luminosity. One can then look at both the intrinsic mass and mass-to-light ratios and those scaled to an L_* galaxy to draw conclusions about the dark matter properties of the different samples.

The basic ideas behind weak lensing are simple. Gravitational lensing distorts the images of background objects (usually galaxies) adjacent on the sky to a foreground mass. The distortion can be split into two terms, the convergence and shear. The convergence term magnifies the background objects by increasing their size, and the shear term stretches them tangentially around the foreground mass. If these distortions can accurately be measured, then the foreground mass can be mapped. To measure this tangential alignment, one must measure the ellipticities of the background galaxies. The main difficulty is that galaxies intrinsically have a distribution of ellipsoidal shapes, so the measured ellipticity is a combination of their intrinsic ellipticity and the gravitational lensing shear. This is not the whole story though, as the shapes of galaxies can be distorted by things other than lensing. For instance, the atmosphere of the Earth and the optics of the camera and telescope can distort the apparent shapes of galaxies.

Many techniques have been developed to proceed from raw measurements taken from images to a final shear estimate (e.g. Kaiser, Squires & Broadhurst (hereafter, KSB), 1995; Bernstein & Jarvis, 2002). Regardless of how the analysis is performed, having very high quality images is advantageous. Wide-field, deep, sub-arcsecond seeing images improve both the statistics and the systematic errors. Generally, weak lensing images are taken in optical bands using a CCD camera. Most images using large cameras are collected using a dither pattern, which allows gaps between CCD chips to be filled and bad pixels removed. Once the images are collected, they must be carefully combined to ensure that the galaxy shapes are not altered by the image stacking procedure. These stacked images are then used for detecting galaxies and measuring their shapes. Basic data reductions, detecting objects in images, shape determination and point-spread-function (PSF) corrections must be done to go from images to galaxy shape (ellipticity) measurements.

Recently, the weak lensing community underwent a large collaborative project called the Shear TEsting Program (STEP) to improve the accuracy and reliability of weak lensing measurements (Heymans et al., 2006; Massey et al., 2007). Their results show that the KSB method refined by Hoekstra et al (1998), as well as the method developed by Bernstein & Jarvis (2002) have minimal systematics and thus weak shear can be measured at percent level accuracy.

There are many ways to detect galaxies and correct their shapes, but the KSB method refined by Hoekstra et al (1998) will be discussed in some detail as it was utilized in the observational project to be discussed futher in Chapters 2-3.

KSB Method

The KSB method has been widely used since it was published in 1995, and many people have added their own improvements to the method (e.g. Hoekstra et al., 1998). The basic idea is that software called imcat implements the KSB method outlined in KSB (1995).[2] Images are smoothed on different scales and 'peaks' are located. The peaks determine the location of objects in the image, and the most significant peak for each object found (looking at all smoothing scales) determines the size of the object. Once objects are located, their shapes are measured. The KSB method parameterizes the shapes (ellipticities) and position angles of objects by the 'vectors' e_1 and e_2 in the x,y coordinate system of the image (see Figure 1.6). Once shapes are observed, the shapes

[2] http://www.ifa.hawaii.edu/ ~kaiser/imcat/content.html

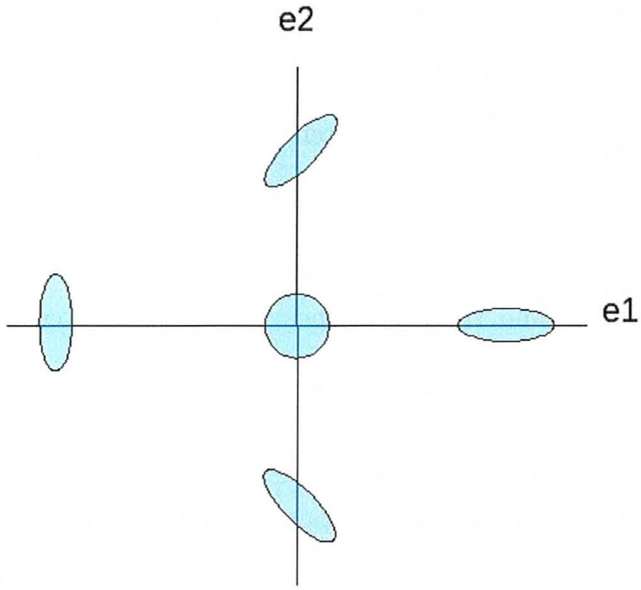

Figure 1.6 e_1 and e_2 parameterize galaxy shapes in weak lensing analysis. These parameters encapsulate both ellipticity and position angle information.

are carefully corrected to account for seeing and any anisotropic PSF features. These techniques have been shown to work well (see Heymans et al., 2006) if there are many stars in the field to aid in calculating the PSF across the field accurately.

Systematic Errors

Whenever weak lensing is used to make an estimate of the shear around a concentration of mass, there exists a built in systematic test. If the phase of the distortion is changed by $\pi/2$ (the equivalent of rotating the source images about their x,y position by 45°) then the resulting shear signal should disappear if the tangential shear signal that was measured is truly due to gravity. This "cross" shear is a quick way to test for some possible systematic effects. We will calculate this cross-shear for our samples in Chapter 3.

Galaxy-Galaxy lensing, and weak lensing in general, relies on the assumption that there are no intrinsic alignments of the background sources with the lenses. If there are potential physical/'real' alignments between the sources and lenses (for example, two galaxies in a filament may be aligned in the same direction), then interpreting a weak lensing signal is complicated by the fact that the galaxies may be part of the same large scale structure. This complication can be removed if redshift information for the lenses and sources is available. Using redshift information, the lens and source samples can have a well defined separation, and one can remove the possible physical association of the lenses and sources. If redshift information is not available, then some sources may actually be satellite galaxies. If satellite galaxies are aligned or anti-aligned to their host galaxy, the tangential shear measurements will be influenced.

Results from the SDSS (Siverd, Ryden & Gaudi, 2009; Augustsson & Brainerd, 2006) suggest that there is a radial alignment between satellites and their hosts, and Siverd et al. (2009) suggest that the nature of the alignment may also depend on the galaxy population. A radial alignment would systematically surpress the tangential lensing signal. Results based on the 2dF Galaxy Redshift Survey indicated that there was no alignment betwen the host galaxy and their satellites, suggesting contamination to a galaxy-galaxy lensing signal due to satellite galaxies would be minimal (Bernstein & Norberg, 2002). These contradictory results indicate the need for photometric or spectroscopic redshifts to clearly separate the lenses and sources.

Summary

Gravitational lensing has an advantage over other observational tools in that it is a method that can directly detect the presence of matter without making any prior assumptions about the dynamics of the system or mass-to-light ratios. While numerical simulations can be used to model the dark matter content of galaxies, and observations look at the luminous content, gravitational lensing is a tool that can look at both the dark and luminous components at the same time. Both strong and weak lensing have many applications. Strong lensing can be used to directly probe the mass distribution of the inner regions of foreground lenses (usually massive elliptical galaxies or clusters), probe dark matter in our own Galaxy through the microlensing of stars in the Milky Way, or to calculate the Hubble constant through the time delay of multiply imaged quasars (Roberts et al., 1991). Weak lensing allows for the detection of dark matter on large scales, but the signal is very small, and understanding the systematic effects and how to correct for them must be carefully accounted for.

The field of gravitational lensing is evolving rapidly and has many applications with much potential. Galaxy-galaxy lensing was first detected in 1996 (Brainerd et al., 1996) and is now a major tool for understanding galaxies, and cosmic shear was first detected in 2000 (Bacon, Refregier & Ellis, 2000; Kaiser et al., 2000; Van Waerbeke et al., 2000; Wittman et al., 2000), and can be used to learn more about dark energy. Weak gravitational lensing, specifically, can be used to probe structures of dark matter and dark energy on scales that other techniques cannot. It can be used to constrain dark matter properties by studying the shapes and sizes of dark matter halos, look for evolution in halos with redshift, and learn more about dark energy by looking at clustering of galaxies.

The remainder of this thesis will deal with galaxy-galaxy lensing using data from the Canada-France-Hawaii Telescope Legacy Survey.

1.4 Thesis Outline

In this thesis I will report on the results of a project that used weak gravitational lensing to probe the mass distributions and properties of galaxy halos. Chapter 2 is a detailed look at the data itself, and the lens samples used for later analysis. In Chapter 3, I will discuss the weak lensing analysis of the various lens samples described in Chapter 2, and infer both the velocity dispersions and masses for the various samples. Mass-to-light ratios have also been calculated for the samples using information about the luminosity of the samples. Finally, in Chapter 4, I will provide a discussion and conclusions based on this work.

Chapter 2

Data & Samples

2.1 CFHTLS

Canada and France agreed to combine a significant fraction (~50%) of their telescope time at the Canda-France-Hawaii-Telescope (CFHT) in order to complete a large 5-year imaging survey (run from 2003 to 2008), called the CFHT Legacy Survey (CFHTLS). The survey made use of the MegaCam instrument at CFHT.[1] The camera is equipped with 36 separate CCD chips and produces distortion corrected 1 square degree images with outstanding image quality. The survey was divided into wide, very wide, and deep components. The wide component was designed primarily for weak lensing studies. The results of the wide study will allow the study of large scale structure in the Universe, and the study of dark matter halos, as well as the study of clusters of galaxies. The shallow component, the very wide survey, was to be used to find and track Kuiper Belt Objects, with the hopes of better understanding the formation and evolution of our solar system but was cut short partway through the survey. The third component, the deep survey, covered 4 square degrees probing

[1] http://www.cfht.hawaii.edu/Instruments/Imaging/MegaPrime/

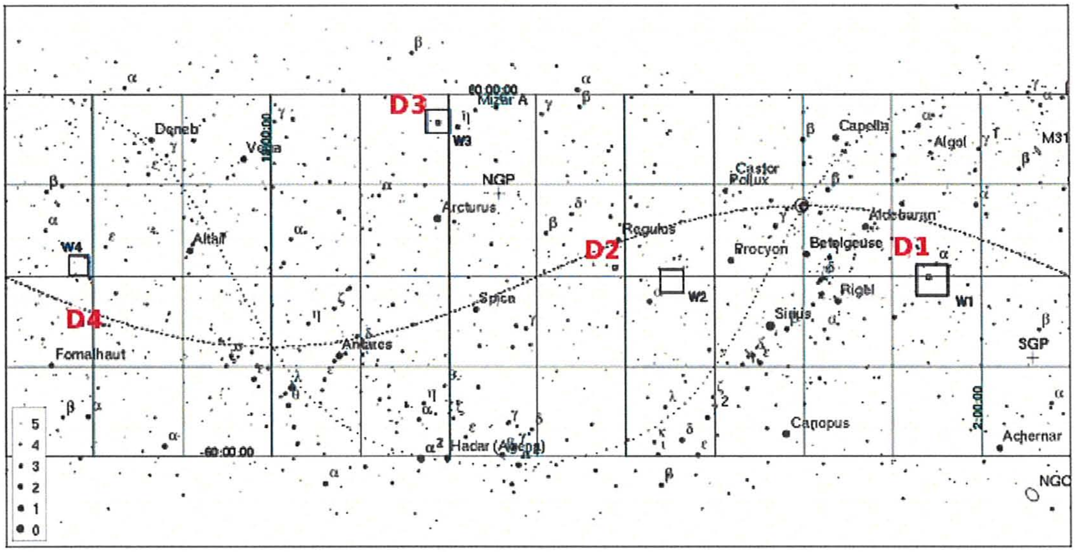

Figure 2.1 : Location of CFHTLS Deep (D1, D2, D3 and D4) and Wide (W1, W2, W3, W4) fields on the Sky

to r' = 28, and its goal was the detection and monitoring of type Ia supernovae in order to better understand the early Universe and determine dark energy parameters with greater accuracy.

This galaxy-galaxy lensing project made use of data from the CFHTLS deep survey. The deep data covers 4 square degrees in 5 filters (u*,g',r',i',z'). The observations are divided into 4 one degree fields which are well-separated in right ascension. Each field is located far from the Galactic plane to minimize extinction and contamination from bright stars. The locations of the wide and deep survey fields can be seen in Figure 2.1.

2.2 Data

The analysis to be presented in Chapter 3 is based on the T0003 release of the CFHTLS deep survey. Only lenses detected in all 5 bands (u*, g', r', i', z') were selected for further analysis. A separation of $\Delta z > 0.5$ between the lenses and sources was adopted to ensure that the lenses and sources were well separated. This value was chosen after some investigation of the number density of sources as a function of angular position for various redshift separations. The galaxy-galaxy lensing analysis was done for subsets of lenses based upon their observed properties: luminosity, colour, and redshift. These subsets and how they were defined are described in detail below.

The CFHTLS images were provided to the Canadian and French astronomical communities after basic reductions (flat-fielding and de-biasing) by the Canadian Astronomical Data Centre. The images also had basic astrometric and photometric calibrations provided. An astrometric correction was applied chip by chip (there are 36 chips in an image), because distortions were fit with polynomials which might have been discontinuous across chips. The corrected images were then carefully stacked together to prevent shape distortions and were then used for weak lensing shape measurements.

The catalogues used in this analysis were created by Ludovic Van Waerbeke using the shape measurement techniques outlined in KSB (1995) and Hoekstra et al. (1998). The catalogues were provided to us with the positions, apparent magnitudes, shapes and errors for each of the 4 deep fields. The catalogues provided by Ludovic Van Waerbeke were carefully matched (using the right ascension and declination of each galaxy) to the photometric redshift catalogue presented in Ilbert et al. (2006) to extract redshifts and absolute magnitudes for the lenses and sources.

2.3 Redshift distribution of Lens and Source Galaxies

For the analysis presented here, we selected a sample of lenses and sources using photometric redshifts from Ilbert et al. (2006). We defined galaxies with $0.2 < z < 1$ as lenses, and galaxies with $z > 0.7$ as sources which were then used to measure the lensing signal. In addition, an apparent magnitude cut of $i' < 24.5$ was applied to the lenses. The redshift distribution of the lenses and sources can be seen in Figure 2.2. This selection yielded a sample of $\sim 1.4 \times 10^5$ lenses and $\sim 2.8 \times 10^5$ sources. These catalogues were used to generate 2.3×10^7 lens-source pairs within a projected radius of 2 arcminutes of the stacked lenses. All sources within 7 arcseconds of the host galaxy were eliminated from the catalogue since their shape measurements might be compromised by light from the host lens.

As previously stated, the lensing signal for an isothermal sphere is a function of $\langle\beta\rangle$, the average weighted ratio (see Chapter 3 section 1 for details of the weighting used) of the angular diameter distances between the lens and source, and the source (equation 1.5). In order to interpret the detected shear measurements it is necessary to know the redshifts of both the lenses and sources. If the redshifts of the lenses and sources are not known for each

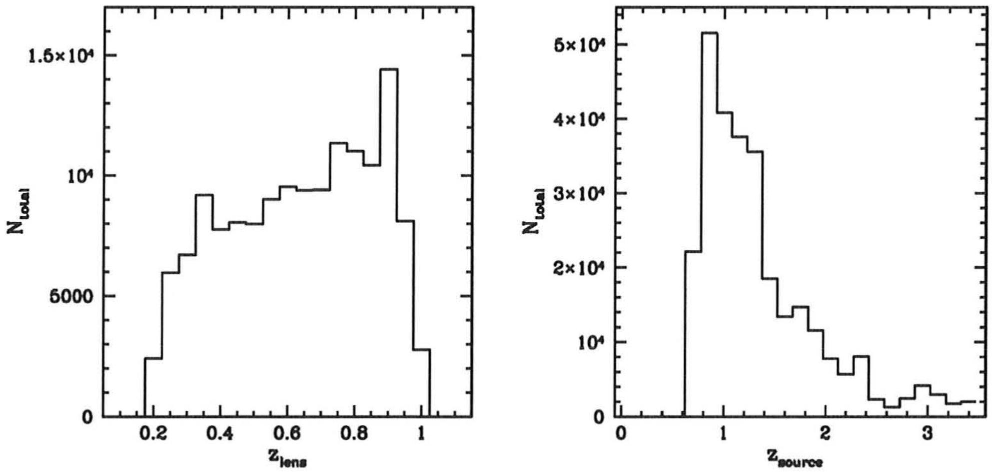

Figure 2.2 : Redshift distribution of lenses and sources in the entire data set. All lenses (*left*) are defined to have redshifts between 0.2 and 1 and the sources (*right*) have redshifts > 0.7. The distribution has been truncated at $z = 3.5$.

object then their distributions must be understood in order to convert shear measurements into properties such as halo mass. If redshifts are available, the shear can be estimated in both projected angular bins and in physical units such as kiloparsecs. Using projected angular bins, the lensing signal for a distant galaxy is measured on a larger physical scale than for a galaxy which is closer, which results in the mixing of scales and complicates the interpretation of results. Despite this complication, we can still learn about the statistical properties of halos.

2.4 Lens Samples

Table 2.1. Sample Characteristics

Sample	# of lenses	# of sources	# of source-lens pairs
All	1.4 x 10^5	2.8 x 10^5	2.3 x 10^7
Red	1.3 x 10^4	2.8 x 10^5	1.9 x 10^6
Green	1.9 x 10^4	2.8 x 10^5	3.3 x 10^6
Blue	1.1 x 10^5	2.8 x 10^5	1.8 x 10^7
Bright ($M_{r'} <$ -22)	9.3 x 10^3	2.8 x 10^5	1.2 x 10^6
Mid (-22 $< M_{r'} <$ -19)	8.6 x 10^4	2.8 x 10^5	1.2 x 10^7
Faint ($M_{r'} >$ -19)	4.8 x 10^4	2.8 x 10^5	9.8 x 10^6
$0.2 < z < 0.6$	6.2 x 10^4	2.8 x 10^5	1.3 x 10^7
$0.6 < z < 1.0$	8.2 x 10^4	2.8 x 10^5	9.5 x 10^6
All [a]	1.4 x 10^5	2.8 x 10^5	9.8 x 10^7
$0.2 < z < 0.6$ [a]	6.2 x 10^4	2.8 x 10^5	7.4 x 10^7
$0.6 < z < 1.0$ [a]	8.2 x 10^4	2.8 x 10^5	2.4 x 10^7

[a] source-lens pairs matched in physical units (kpc) instead of angular units ["]

Here we describe the various samples used in the analysis in Chapter 3, and how they were defined. Table 2.1 shows the number of lenses, sources and source-lens pairs calculated for each sample.

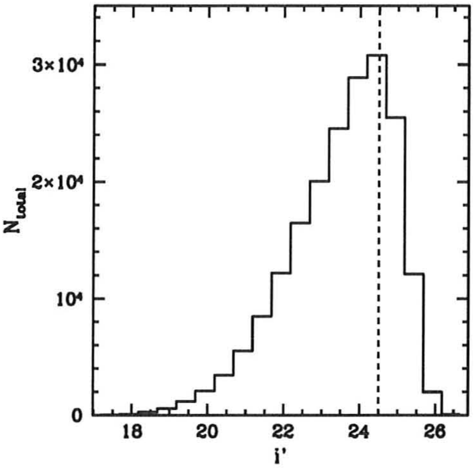

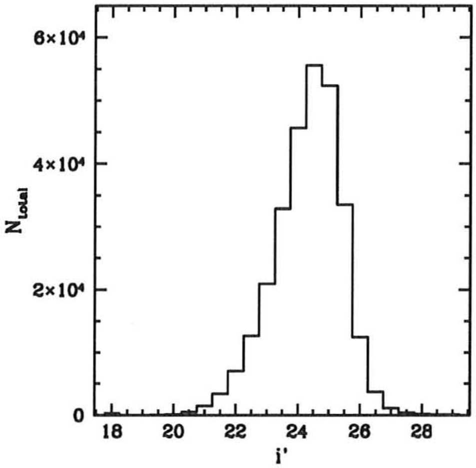

Figure 2.3 : Apparent i' magnitude distribution of lenses and sources for the entire data set. The lenses, (*left*) had a cut made at i' = 24.5 such that only lenses brighter than i' = 24.5 were kept in the final lens sample. (*right*) The apparent i' magnitude distribution for the sources.

2.4.1 Entire Sample

The entire lens sample was described above. All lenses have redshifts between 0.2 and 1 and a magnitude cut of i' < 24.5 was applied. This yielded a sample of $\sim$ 1.4 x 10^5 lenses. Figure 2.3 shows the magnitude distribution for the entire sample of lenses and sources used in this analysis.

As redshift information was available for this analysis, the entire sample was also used to estimate the shear in physical units. The catalogues were used to create $\sim$ 9.8 x 10^7 source-lens pairs within 1 Megaparsec of the stacked lenses. All source-lens pairs within 50 kiloparsecs of the host galaxy were eliminated from the catalogue as their shape measurements were likely compromised by light from the host lens.

2.4.2 Colour Sample

The CFHTLS deep has information in 5 filters available, so colour magnitude diagrams (CMDs) for the lens galaxies could be created to divide the lenses by colour. A colour magnitude diagram was created using absolute magnitudes instead of apparent ones to try to minimize any evolution in colour with redshift. Figure 2.4 shows the colour magnitude diagram of the entire sample of lenses in $M_{g'}$ - $M_{r'}$ vs. $M_{r'}$. The colour magnitude diagram was generated by Greg Stinson.

Using the colour magnitude diagram, the lenses were divided into 3 colour bins, red, green and blue. The red sequence and blue cloud can be clearly seen in Figure 2.4, but we also consider a third intermediate population in between called the green valley (see Wyder et al., 2007). Figure 2.5 shows the colour distribution for the lenses. Red lenses were defined to have an absolute colour of $M_{g'}$ - $M_{r'}$ > 0.55, blue lenses an absolute colour of $M_{g'}$ - $M_{r'}$ < 0.4, and green lenses 0.4 < $M_{g'}$ - $M_{r'}$ < 0.55. The redshift and i' apparent magnitude distributions for the red, green and blue lenses can be seen in Figure 2.6.

2.4.3 Luminosity Sample

As absolute magnitude information was available, the lenses could be divided by their luminosity. Using r' absolute magnitudes, the lenses were divided into 3 luminosity bins, bright, intermediate and faint. Figure 2.7 displays the r' band absolute magnitude distribution for the lenses. The bright lenses were defined to have $M_{r'}$ < -22, the intermediate sample to have -19 < $M_{r'}$

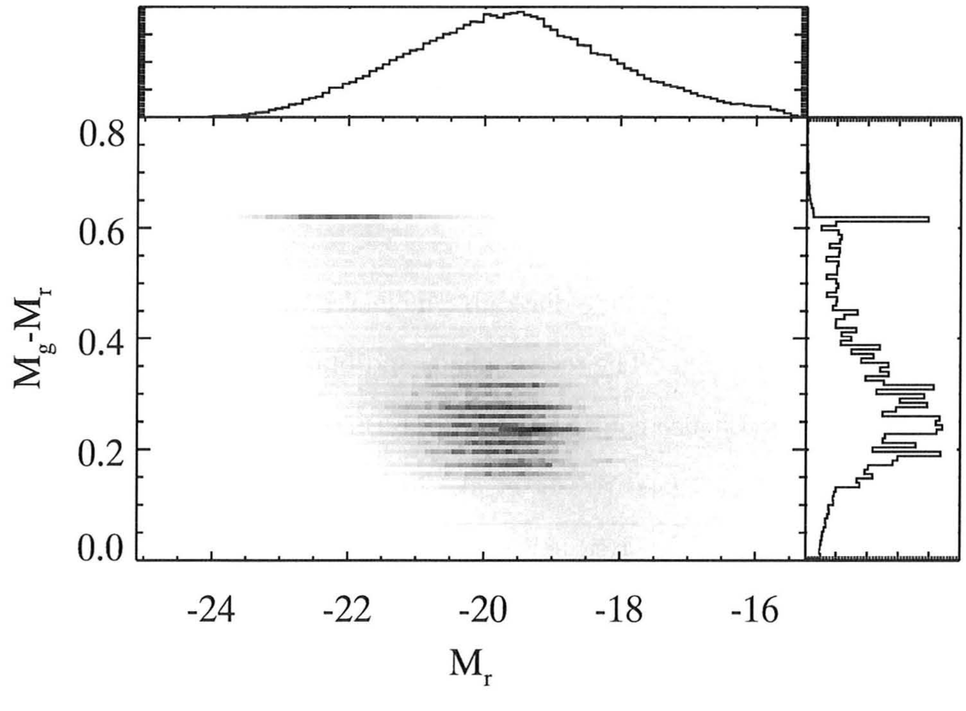

Figure 2.4 : Colour Magnitude Diagram of the lens galaxies. Plot in absolute colour $M_{g'}$ - $M_{r'}$ vs. absolute magnitude $M_{r'}$. The primes need to be added to the figure. The bi-modal distribution of the red sequence and blue cloud can clearly be seen. We also consider a third, intermediate population in between called the green valley. Figure generated by Greg Stinson, McMaster University

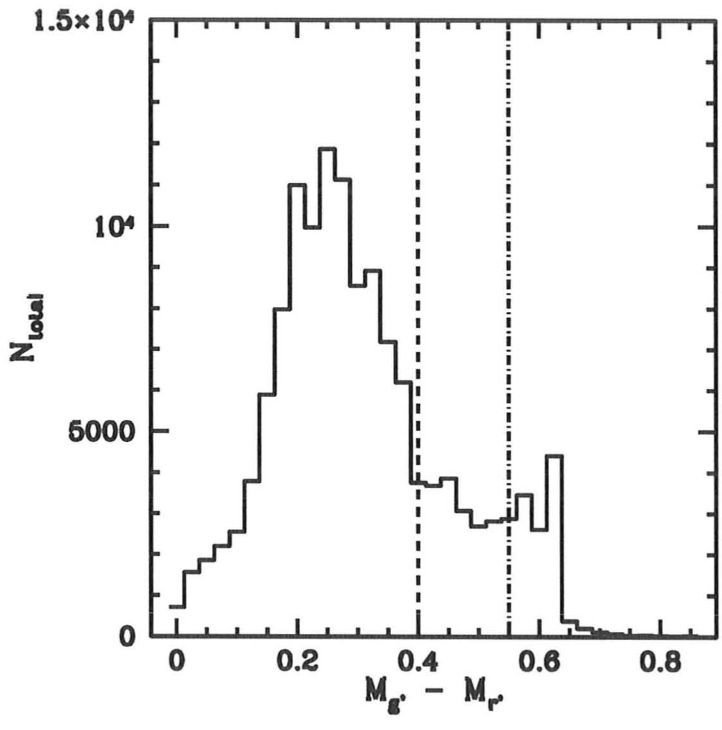

Figure 2.5 : Colour histogram of the lens galaxies. The cuts to define the red, blue and green lens samples are indicated. Red lenses have an absolute colour $M_{g'}$ - $M_{r'}$ > 0.55, blue lenses have an absolute colour $M_{g'}$ - $M_{r'}$ < 0.4 and the green lenses are defined as the region in between, 0.4 < $M_{g'}$ - $M_{r'}$ < 0.55.

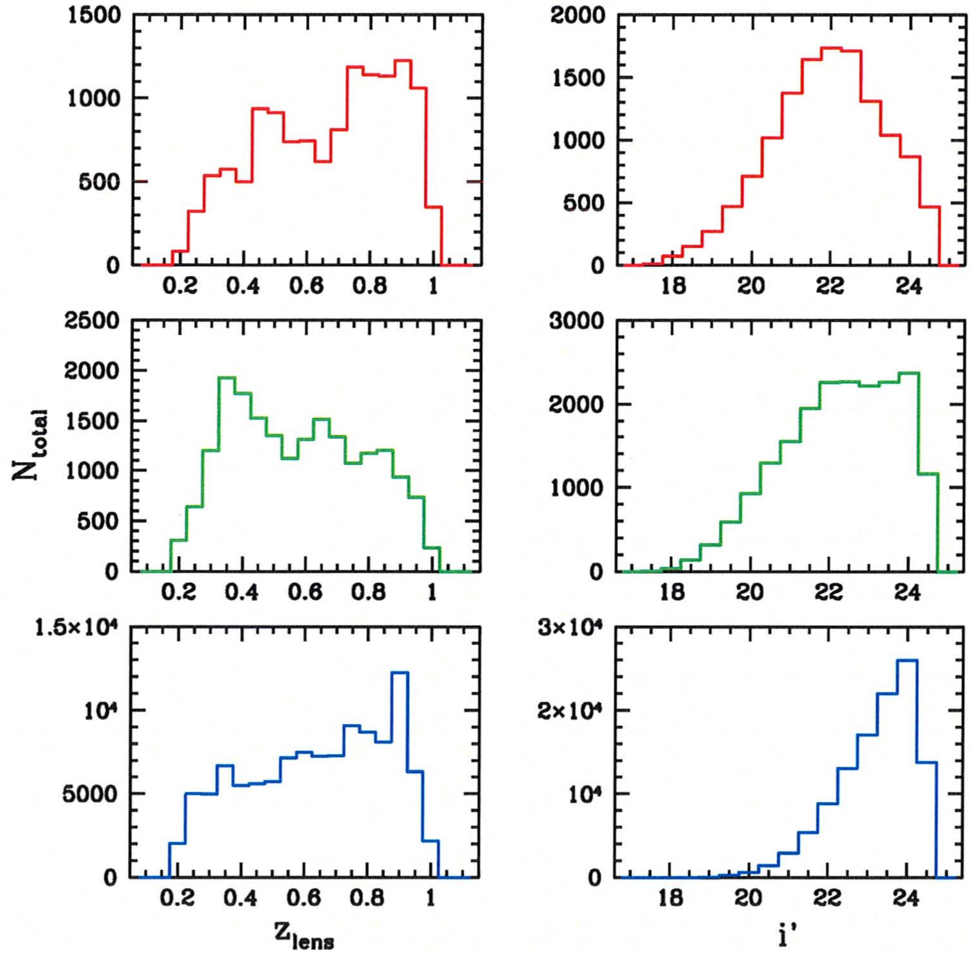

Figure 2.6 : Histograms of the colour divided lens sample. The histograms on the *left* indicate the redshift distribution of the red (*top*), green (*middle*), and blue (*bottom*) samples respectively. The histograms on the *right* show the apparent i' magnitude distribution of the red, green and blue samples.

< -22, and the faint sample to have $M_{r'}$ > -19. The apparent i' magnitudes and redshift distributions for the luminosity samples can be seen in Figure 2.8. The bright and intermediate samples can be seen to have higher average redshifts than the faint sample, and as expected, the apparent i' magnitudes are fainter for the faint sample than the intermediate and the bright samples.

Aside from learning more about the masses of dark matter halos for a luminosity divided sample, one can also use this information to try to plot a total mass Tully-Fisher relation, as the masses calculated are for the total mass of the halo, which is not always easy to estimate from rotation curves. A "total mass" Tully-Fisher relation will be investigated further in Chapter 3.

2.4.4 Redshift Sample

Having redshift information available makes studies of halo evolution possible. We attempt to measure halo evolution by dividing the lenses into various high and low redshift samples and comparing them to look for differences. One such division into high and low redshift was a low redshift sample of $0.2 < z < 0.6$ and a high redshift sample of $0.6 < z < 1$. One can also divide the lenses by applying a colour cut to use only red lenses.

While evolution studies can be done using projected angular separations of sources and lenses, it also makes sense to look at evolution using physical units. Using physical units would prevent the mixing of scales for the lenses making the interpretation of results less complicated. We have created source lens pairs using physical units for redshift samples of $0.2 < z < 0.6$ and 0.6

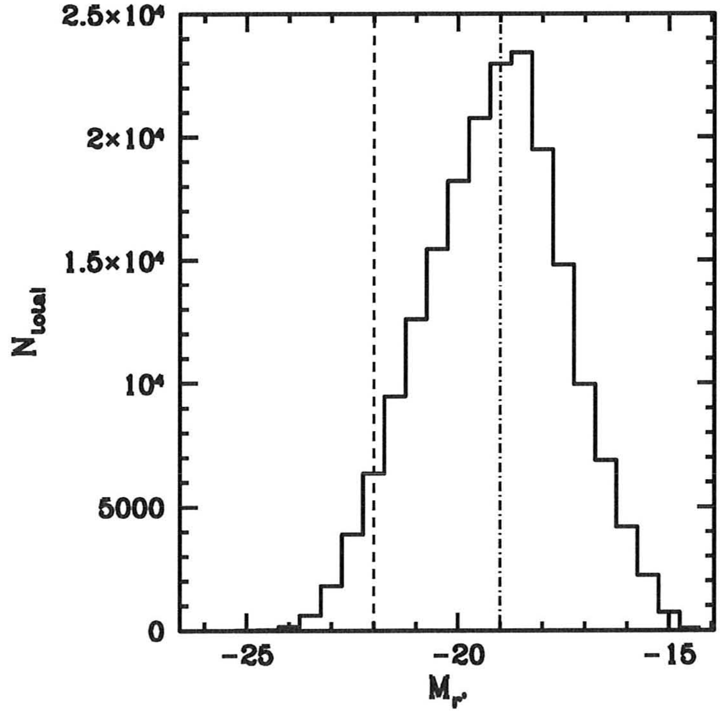

Figure 2.7 : Histogram describing the luminosity divided sample of lenses. The bright lenses have $M_{r'}$ < -22, the faint sample is defined with $M_{r'}$ > -19, and the intermediate sample is located in between.

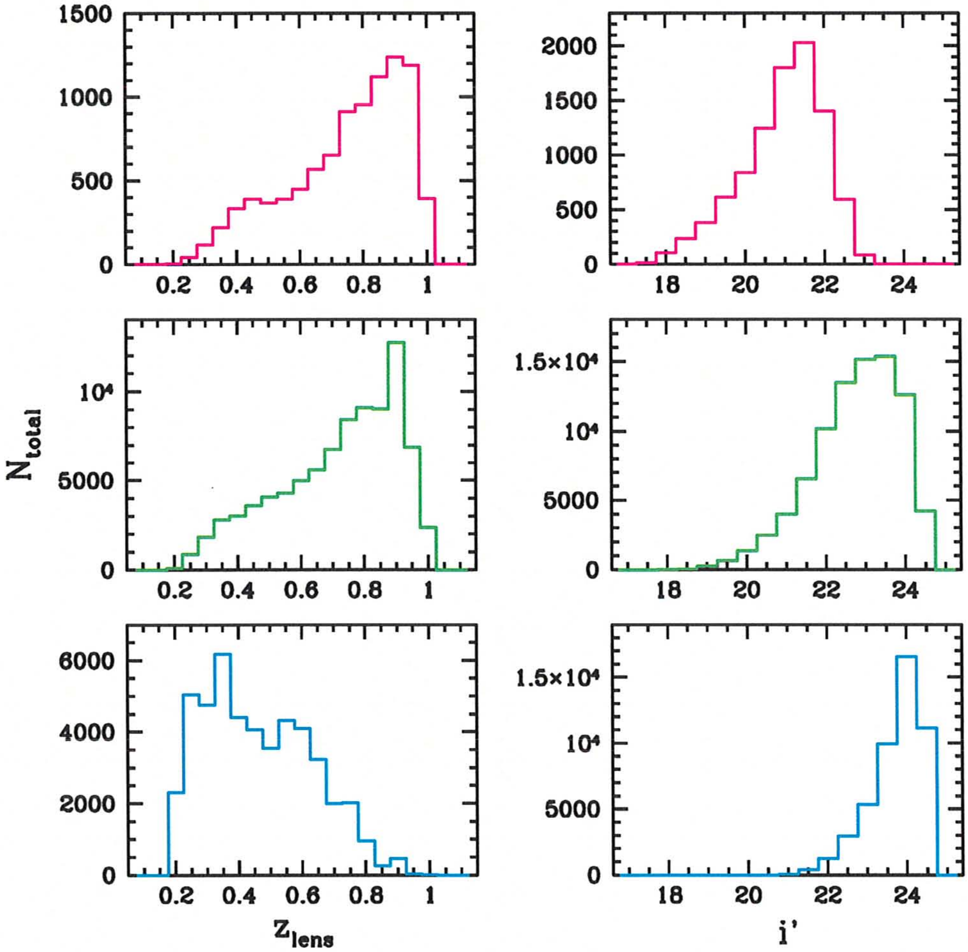

Figure 2.8 : Histograms of the luminosity divided lens sample. The histograms on the *left* indicate the redshift distribution of the bright (*top*), intermediate (*middle*), and faint (*bottom*) samples. The histograms on the *right* show the apparent i' magnitude distribution of the three samples.

$< z < 1$ to compare the use of projected angular bins to physical units when looking at halo evolution.

Chapter 3

Analysis & Results

In this chapter we present our galaxy-galaxy lensing analysis of luminosity, colour, and redshift lens samples, as well as an analysis for the entire lens sample. The entire sample and redshift samples were analysed in both angular and physical units. As we will demonstrate, there is very strong weak lensing signal detected with our data set. We also present measurements of the projected shapes of galaxy halos. We first present a basic analysis, describing how the lensing measurements were made, and how various values were computed, then we discuss our results, including halo evolution and halo shape measurements.

In this work values of $H_0 = 100$ km s^{-1} Mpc^{-1}, $\Omega_m = 0.3$ and $\Omega_\Lambda = 0.7$ were adopted (see Table 3.1 for an explanation of these parameters), but everything is quoted in terms of h. For lensing samples calculated in angular units, the maximum separation adopted was 2'. For those in physical units, we probed out to separations of 1 h^{-1}Mpc.

Symbol	Name	Description
H_0	Hubble Constant	Describes the current expension rate of the Universe, in units of km s^{-1} Mpc^{-1}
ρ_c	Critical Density	Density required to make the Universe spatially flat $\frac{3H_0^2}{8\pi G}$
Ω_Λ	Vacuum density	The normalized energy density of vacuum (dark energy or cosmological constant). $\Omega_\Lambda = \rho_\Lambda/\rho_c$
Ω_m	Matter Density	The normalized density of luminous and dark matter in the Universe. $\Omega_m = \rho_m/\rho_c$
h	Hubble parameter	Rescaled Hubble constant, in units of 100 km s^{-1} Mpc^{-1}

Table 3.1 Cosmological Parameters

3.1 Basic Analysis

The lenses are stacked together and the sources that lie within a projected radius of 2 arcminutes (or physical distance of 1 h^{-1}Mpc) are divided into angular (or physical distance) bins. The component of the source shape tangential to the lens centre is determined and a weighted average calculated in each bin. Each shear calculation is weighted by the error in the shape measurement as described in Hoekstra et al. (2000) such that galaxies that are fainter and have poor shape measurements are down-weighted.

The tangential shear profile (which is an indicator of gravitational lensing) can then be fit with an isothermal sphere model given by

$$\gamma_T = \frac{\theta_E}{2\theta} = \frac{2\pi\sigma^2}{c^2\theta}\beta \tag{3.1}$$

where θ is the angular separation of the lens and source, in order to estimate the Einstein radius.

The tangential shear is proportional to the Einstein radius and hence to the velocity dispersion squared for an isothermal sphere potential (equation 1.4). The velocity dispersion depends on the sample of lenses and must be scaled in order to compare to other results. A comparison can easily be done by assuming a scaling relation between velocity dispersion and luminosity as follows

$$\frac{\sigma}{\sigma_*} = \left(\frac{L}{L_*}\right)^{1/\alpha} \tag{3.2}$$

where σ_* is the velocity dispersion of an L_* galaxy. The scaling factor α is generally assumed to be 3 or 4, motivated by the Faber-Jackson (Faber & Jackson, 1976) or Tully-Fisher relations (Tully & Fisher, 1977), for example. As our galaxy sample ranges from 0.2 - 1 in redshift and we were looking for signs of evolution, we adopted an L_* galaxy that evolves with redshift in the following way. Using the VLT-VIMOS luminosity function results of Zucca et al. (2006), we computed M^* in B-band from their M^*_{AB} in the B-band using corrections from Frei & Gunn (1994) and using the proportion of galaxy types for each redshift bin, to calculate L_* for galaxies in the range of $0.2 < z < 0.4$, $0.4 < z < 0.6$, $0.6 < z < 0.8$ and $0.8 < z < 1$. We used the B-band absolute magnitudes from Ilbert et al. (2006) to calculate the luminosity of our galaxy samples and the estimated L_* from Zucca et al. (2006) for the average redshift, to compute the scaled velocity dispersion for different assumed α values. The values for the average luminosity $\langle L \rangle$, adopted L_*, average weighted redshift $\langle z \rangle$, weighted $\langle \beta \rangle$, and the results of scaling the observed σ for our samples of lenses to the given L_* can be seen in Table 3.2. Note, that $\langle z \rangle$, and $\langle \beta \rangle$

were weighted using the same weights as the shear, following Hoekstra et al. (2000).

To determine the total mass and extent of dark matter halos, one can assume a mass model for the galaxy halos such as that suggested by Brainerd, Blandford, and Smail (1996) which has a density profile of

$$\rho(r) = \frac{\sigma^2 s^2}{2\pi G r^2 (r^2 + s^2)} \tag{3.3}$$

where s is a measure of the truncation scale of the halo. This is an isothermal sphere profile at small radii with a cut-off at large radii, which is characterized by the truncation scale s, which scales with velocity dispersion (Schneider & Rix, 1997)

$$s = s_* \left(\frac{\sigma}{\sigma_*}\right)^2 \tag{3.4}$$

Assuming this truncated isothermal sphere halo model, the mass enclosed within a sphere of radius r is

$$M(r) = \frac{2\sigma^2 s}{G} arctan \left(\frac{r}{s}\right) \tag{3.5}$$

which, due to the truncation, results in a finite mass (Hoekstra et al., 2004)

$$M_{tot} = \frac{\pi\sigma^2 s}{G} = 7.3 \times 10^{12} \left(\frac{\sigma}{100kms^{-1}}\right)^2 \left(\frac{s}{1Mpc}\right) \tag{3.6}$$

We assume the truncation radius found by Hoekstra, Yee & Gladders (2004) for an L_* galaxy of 185 ± 30 kpc, for determination of halo masses.

3.2 Basic Results

3.2.1 Full Sample

The tangential and "cross" shear for the entire lens sample calculated in radial bins is plotted in Figure 3.1. These data are best fit with an isothermal sphere with an Einstein radius of 0".115 $\pm$ 0".009. A lensing signal is detected with high significance ($> 12\sigma$). The cross shear measurement is consistent with zero as expected, and therefore the tangential lensing signal is interpreted as being caused by weak lensing from an isothermal sphere potential.

The tangential shear for the entire lens sample calculated in physical bins is shown in Figure 3.2. These data are best fit by an isothermal sphere potential with an Einstein radius of 0".168 $\pm$ 0".023. A lensing signal is detected with high significance ($> 7\sigma$). It should be noted that an isothermal sphere model does not fit the data well in the inner regions when the data are plotted in physical units. Alternative mass models such as a Navarro, Frenk and White (NFW) profile (Navarro, Frenk & White, 1996), may fit better, although this was not explored here.

The best-fit Einstein radius for the entire sample calculated in angular bins (Figure 3.1) yields a velocity dispersion of 85 $\pm$ 7 km s^{-1}. The entire sample when computed in physical units had a velocity dispersion of 98 $\pm$ 13 km s^{-1}. These samples of lenses have an average redshift of 0.54 and 0.45 for the angular and physical scales, respectively. We estimate the average luminosity for our lens galaxies to be $\langle L \rangle = 4.79$ x $10^9 h^{-2}\mathrm{L}_{\odot B}$ for the entire sample computed in angular bins, and $\langle L \rangle = 3.07 \times 10^9 h^{-2} L_{\odot B}$ for the entire sample computed in physical units.

We estimate the total mass of an L_* galaxy for the entire sample to be $1.7 \pm 0.3 \times 10^{12} h^{-1} M_\odot$ if $L \propto \sigma^3$ and $1.5 \pm 0.3 \times 10^{12} h^{-1} M_\odot$ if $L \propto \sigma^4$ when computed in angular bins. If we compute the total mass in physical units, our L_* galaxy has an estimated mass of $3.1 \pm 0.7 \times 10^{12} h^{-1} M_\odot$ if $L \propto \sigma^3$ and $2.5 \pm 0.5 \times 10^{12} h^{-1} M_\odot$ if $L \propto \sigma^4$. The results agree with the results from Parker et al. (2007) which found the total halo mass to be $2.4 \pm 0.5 \times 10^{12} h^{-1} M_\odot$ for $L \propto \sigma^3$ and $2.2 \pm 0.4 \times 10^{12} h^{-1} M_\odot$ for $L \propto \sigma^4$ when computed in angular bins. It should be noted that the data used in this analysis cover a wide range in redshift ($0.2 < z < 1$), which may explain the differences in the results.

Using the luminosity of an L_* galaxy together with the estimated total mass computed from the velocity dispersion, a typical M/L ratio can be calculated. The M/L ratio for the entire sample when computed in angular bins was $154 \pm 28\ hM_\odot/L_{\odot B}$ and $133 \pm 24\ hM_\odot/L_{\odot B}$ for $\alpha = 3$ and 4, respectively. Values of M_{tot} for an L_* galaxy with $\alpha = 3$ or 4, M_{tot}, M_*/L_*, and M/L for all samples can be found in Table 3.2.

3.2.2 Colour

The tangential shear for the red, green and blue lens samples calculated in angular bins are plotted in Figure 3.3. The colours used to define the samples were defined above, and can be seen in Figure 2.5. The best fit isothermal sphere yields an Einstein radius of 0".386 ± 0".044, 0".141 ± 0".014, and

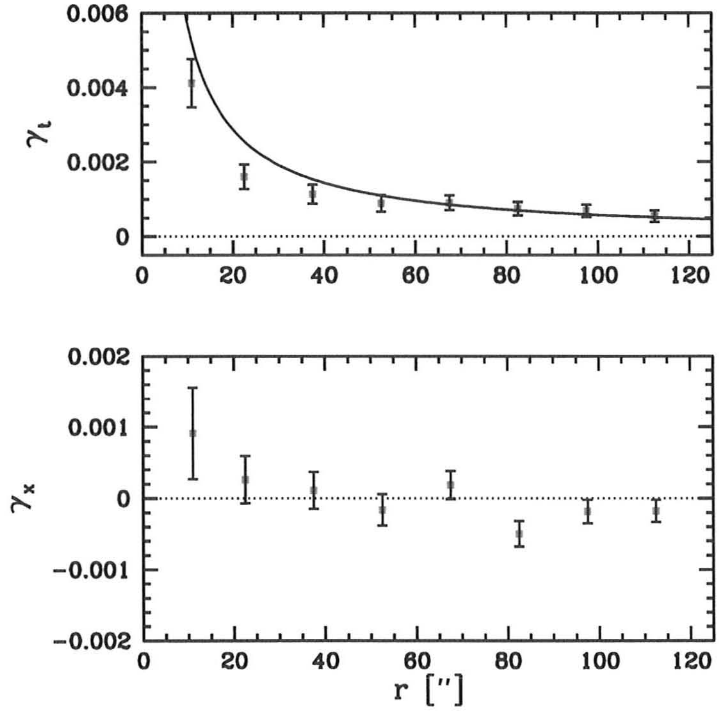

Figure 3.1 : (*top*) The ensemble-averaged tangential shear as a function of radius around a sample of CFHTLS galaxies with i' < 24.5. The best fit isothermal sphere, shown with the solid line, yields an Einstein radius of 0".115 $\pm$ 0".009, corresponding to a velocity dispersion of 85 $\pm$ 7 km s^{-1}. (*bottom*) The signal when the source images are rotated by 45°. Note the difference in scales between the top and bottom figures. The distribution of γ_x with r" is consistent with no trend and zero mean, as expected if the signal from (*top*) is due to gravitational lensing.

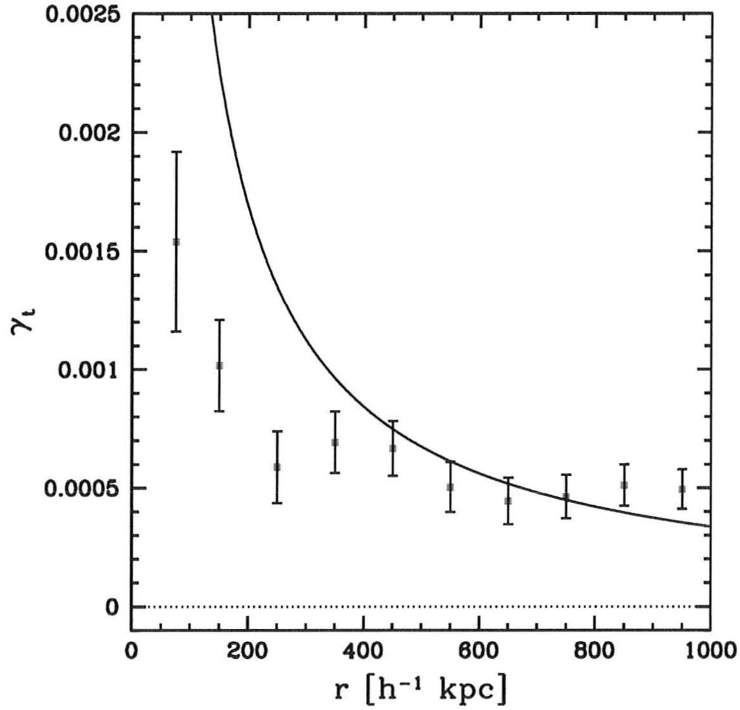

Figure 3.2 : The ensemble-averaged tangential shear as a function of physical distance for a sample of CFHTLS galaxies with i' < 24.5. The best fit isothermal sphere, shown with the solid line, yields an Einstein radius of 0".168 $\pm$ 0".023, corresponding to a velocity dispersion of 98 $\pm$ 13 km s^{-1}.

0".080 $\pm$ 0".009, for the red, green and blue samples, respectively. A lensing signal is detected with high significance ($> 8\sigma$, $> 10\sigma$ and $> 8\sigma$) for each sample.

The red, green and blue lenses had best fit Einstein radii (Figure 3.3) which yielded velocity dispersions of 159 $\pm$ 18 km s^{-1}, 93 $\pm$ 9 km s^{-1}, and 71 $\pm$ 8 km s^{-1}, respectively. These lens samples have average redshifts of 0.58 for the red, 0.50 for the green and 0.55 for the blue. We estimate the average luminosity of these lens galaxies to be $\langle L \rangle$ = 1.61 x $10^{10}h^{-2}$L$_{\odot B}$ for the red sample, $\langle L \rangle$ = 7.20 x $10^{9}h^{-2}$L$_{\odot B}$ for the green sample, and $\langle L \rangle$ = 3.88 x $10^{9}h^{-2}$L$_{\odot B}$ for the blue sample.

3.2.3 Luminosity

The tangential shear for the bright, intermediate and faint lens samples calculated in angular bins are shown in Figure 3.4. The absolute magnitudes used to define the samples can be seen in Figure 2.7. These data are best fit with an isothermal sphere with an Einstein radius of 0".333 $\pm$ 0".017, 0".159 $\pm$ 0".015, and 0".039 $\pm$ 0".008, for the bright, intermediate and faint samples, respectively. A lensing signal is detected with high significance ($> 19\sigma$, $> 10\sigma$ and $> 4\sigma$) for each sample. The samples are distinct from one another at $> 4.5\sigma$.

For the luminosity selected sample, we computed the velocity dispersions for the best fit Einstein radii and this yielded values of 154 $\pm$ 8 km s^{-1}, 105 $\pm$ 10 km s^{-1}, and 47 $\pm$ 9 km s^{-1} for the bright, intermediate and faint

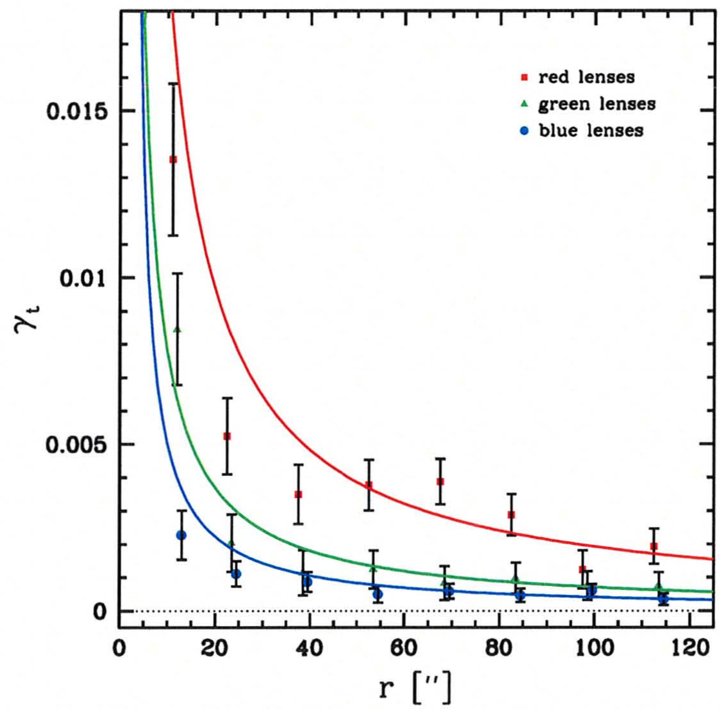

Figure 3.3 : The ensemble-averaged tangential shear as a function of radius around a sample of CFHTLS galaxies divided by colour (see Figure 2.5). The best fit isothermal sphere, shown with the solid line, yields an Einstein radius of 0".386 ± 0".044, 0".141 ± 0".014, and 0".080 ± 0".009, for the red, green and blue samples respectively. The corresponding velocity dispersions are 159 ± 18 km s^{-1}, 93 ± 9 km s^{-1}, and 71 ± 8 km s^{-1}.

samples respectively. These lenses have average redshifts of 0.68, 0.65 and 0.41. The average luminosity for the bright, intermediate and faint samples were estimated to be $\langle L \rangle$ = 7.22 x $10^{11}h^{-2}L_{\odot B}$, $\langle L \rangle$ = 1.15 x $10^{11}h^{-2}L_{\odot B}$ and $\langle L \rangle$ = 1.29 x $10^{10}h^{-2}L_{\odot B}$.

As we were able to divide our lenses into 3 distinct luminosity samples, we were able to compute a Tully-Fisher (TF) relation. The Tully-Fisher relation is a correlation between the maximum circular velocity v_{circ} of a galaxy and its luminosity. To compute a "total mass" TF relation, we converted our velocity dispersions to circular velocities using

$$v_{circ} = \sqrt{2}\sigma \tag{3.7}$$

(Peebles, 1993). Using the estimated luminosities for these three samples of galaxies and their calculated circular velocities, a log-log plot of B-band luminosity (in $L_{\odot B}$) versus circular velocity (in km s^{-1}) was computed. A weighted least squares fit to the data yielded a best fit with $\log(L_{\odot B}) \propto 3.7$ ($\pm$ 0.4) $\log(v_{circ})$. The results can be seen in Figure 3.5.

From the virial theorem, one can derive the Tully-Fisher relation to see the scaling between luminosity and circular velocity as follows: The virial theorem states that for gravitationally bound systems in equilibrium, twice the total kinetic energy (K) of the system is equal to the negative of the total potential energy (W) of the system, or W = -2K where W and K are defined as:

$$W = \frac{-GM}{R}, K = \frac{1}{2}M\langle v^2 \rangle \tag{3.8}$$

For flat rotation curves, this yields:

$$M = \frac{v_{max}^2 R}{G} \tag{3.9}$$

To relate the mass M to the luminosity L of the galaxy, let $\Upsilon = M/L =$ constant, so that

$$L = \frac{v_{max}^2 R}{\Upsilon G} \tag{3.10}$$

If we assume that all spiral galaxies have the same surface brightness I_0 so that $L = \pi R^2 I_0$, then we get:

$$L = \frac{1}{\pi G^2 \Upsilon^2 I_0} v_{max}^4 \tag{3.11}$$

which reproduces the scaling of the Tully-Fisher relation L $\propto v_{max}^4$.

Comparing our results to that of the Tully-Fisher relation derived from the virial theorem, our results yield a scaling of L $\propto v_{max}^{3.7\pm0.4}$, which is consistent with theoretical predictions. Observational work using rotation curves can only probe the luminous component of galaxies. In principle, v_{max} probes the total mass of a galaxy, but this is hard to measure and is subject to fitting and some dynamical assumptions as we do not know what happens to v(r) for r > $\mathrm{r}_{observed}$. TF relations generally have yielded values of L $\propto v_{max}^{\alpha}$ where $\alpha \sim 3$ (e.g. De Rijcke et al., 2007). Only gravitational lensing, and specifically weak lensing, allows us to probe the outer extent of galaxies to compute a TF relation without having to make any dynamical assumptions.

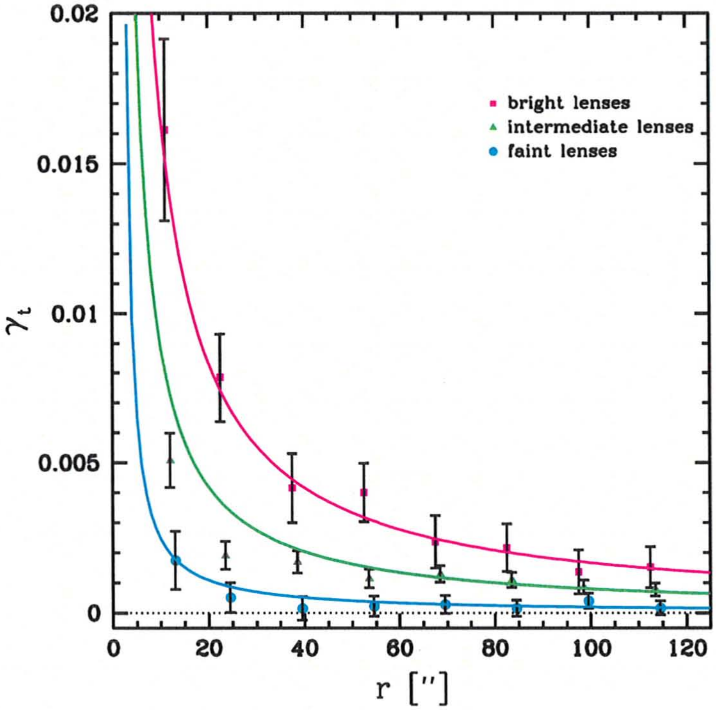

Figure 3.4 : The ensemble averaged tangential shear as a function of radius around a sample of CFHTLS galaxies divided by luminosity (see Figure 2.7). The best fit isothermal sphere, shown with the solid line, yields an Einstein radius of 0''.333 $\pm$ 0''.017, 0''.159 $\pm$ 0''.015, and 0''.039 $\pm$ 0''.008, for the bright, intermediate and faint samples respectively. The corresponding velocity dispersions are 154 $\pm$ 8 km s^{-1}, 105 $\pm$ 10 km s^{-1}, and 47 $\pm$ 9 km s^{-1}.

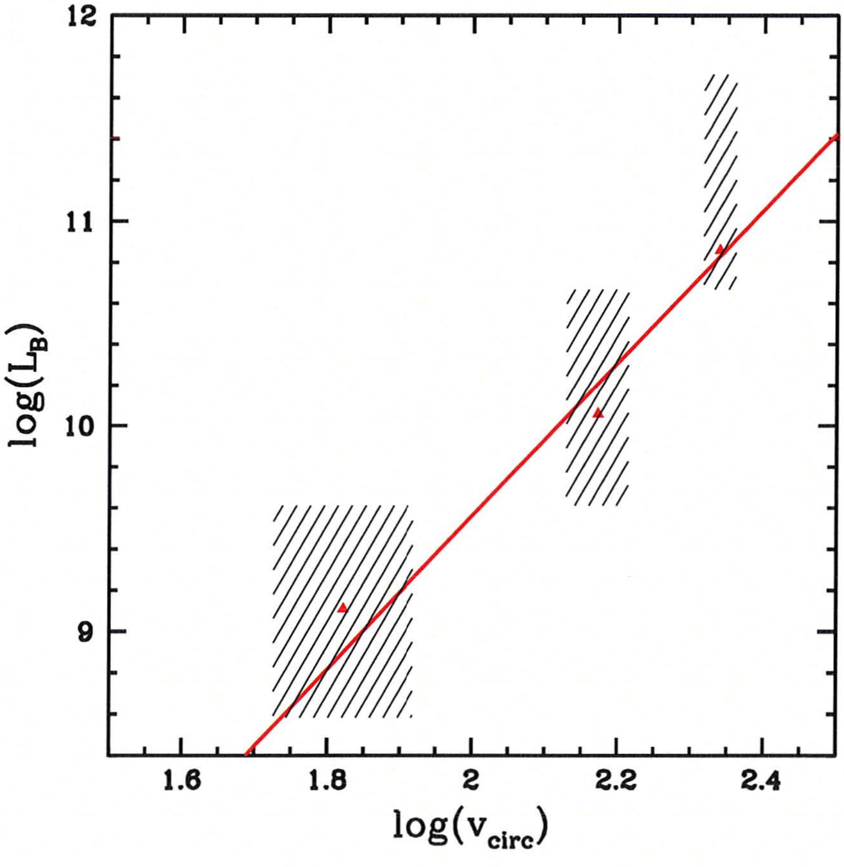

Figure 3.5 : A log-log plot of B-band luminosity (in $L_{\odot B}$) versus circular velocity (in km s^{-1}). A weighted least squares fit to the data yielded a best fit with $L_B \propto v_{circ}{}^{3.7\pm0.4}$ which is consistent with theoretical predictions. The shaded regions show the uncertainties in log(v_{circ}), and the upper and lower limits for each of the luminosity bins.

3.3 Halo Evolution

In searching to see if there is any evolution in dark matter halos over time, we calculated the tangential shear for a high and low redshift lens sample in angular bins which can be seen in Figure 3.6. The high redshift sample was defined to have a redshift in the range of 0.6 - 1.0 and the low redshift sample a range of 0.2 - 0.6. These data were fit with an isothermal sphere model and the best-fit Einstein radius was 0".431 $\pm$ 0".050, for the high redshift sample, and 0".351 $\pm$ 0".069, for the low redshift sample. A lensing signal is detected with high significance ($> 8\sigma$ and $> 5\sigma$) for the high and low redshift samples. To draw conclusions about whether dark matter halos evolve over time, one must look at the velocity dispersions and halo masses once they have been scaled to one another by scaling to an $L*$ galaxy, so that the same populations of galaxies are being compared to one another. This will be discussed below in more detail.

The tangential shear results for the same redshift samples computed in physical units can be seen in Figure 3.7. The shear is best fit by an isothermal sphere with an Einstein radius of 0".140 $\pm$ 0".016 and 0".189 $\pm$ 0".031, for the high and low redshift samples respectively. While the fit to the data is poor in the inner regions especially for the low redshift sample, the lensing signal is still detected at high significance for both samples at $> 8\sigma$ and $> 5\sigma$ for the high and low redshift samples respectively.

The best fit Einstein radius for the redshift sample calculated in angular bins (Figure 3.6) yields a velocity dispersion of 186 $\pm$ 21 km s^{-1} for the high redshift sample, and 141 $\pm$ 28 km s^{-1} for the low redshift sample. When the velocity dispersions were computed in physical units for these same 2 samples, the results were 105 $\pm$ 12 km s^{-1}, and 100 $\pm$ 16 km s^{-1}. These samples of lenses have average redshifts of 0.39 and 0.78 for the low and high redshift samples computed in angular bins and 0.35 and 0.76 when computed in physical units. We estimate the average luminosity for our lens galaxies to be $\langle L\rangle$ = 2.71 x $10^9 h^{-2}$L$_{\odot B}$ and $\langle L\rangle$ = 1.14 x $10^{10} h^{-2}$L$_{\odot B}$ for the low and high redshift samples computed in angular bins, and $\langle L\rangle$ = 2.11 x $10^9 h^{-2}$L$_{\odot B}$ and $\langle L\rangle$ = 1.20 x $10^{10} h^{-2}$L$_{\odot B}$ when computed in physical units. We explored various redshift bins but we present only the results for the bins described above.

We computed the total mass for our L$_*$ galaxy for our high and low redshift samples in both angular and physical bins, searching for possible signs of evolution in dark matter halos. For the sample computed in angular bins, we see no signs of evolution. This result is consistent with previous results (Wilson et al., 2001; Parker et al., 2007). For the sample computed in physical units, there is a $\sim 1\sigma$ difference seen between the high and low redshift samples. We find a total mass of 3.4 $\pm$ 0.8 x $10^{12} h^{-1}$M$_\odot$ if L $\propto \sigma^3$ and 2.7 $\pm$ 0.6 x $10^{12} h^{-1}$M$_\odot$ if L $\propto \sigma^4$, for the low redshift sample and a total mass of 1.6 $\pm$ 0.3 x $10^{12} h^{-1}$M$_\odot$ if L $\propto \sigma^3$ and 1.5 $\pm$ 0.3 x $10^{12} h^{-1}$M$_\odot$ if L $\propto \sigma^4$ for the high redshift sample. These results indicate the need to exercise caution when interpreting weak lensing results where a broad range in redshift is being used, and how the mixing of scales by using angular bins can yield different results than when using redshift information to compute the tangential shear in physical units.

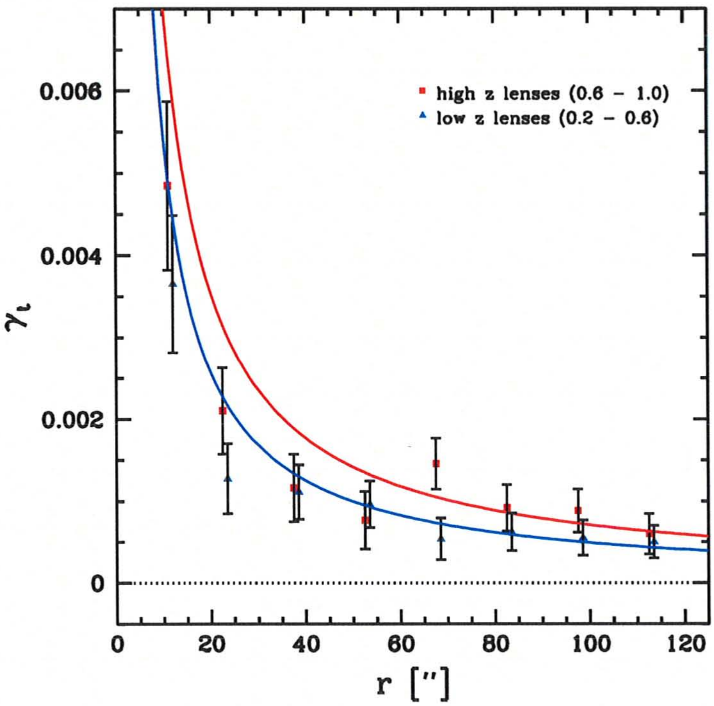

Figure 3.6 : The ensemble-averaged tangential shear as a function of radius around a sample of CFHTLS galaxies divided by redshift. The best-fit isothermal sphere, shown with the solid line, yields an Einstein radius of 0".431 $\pm$ 0".050, for the high redshift sample, and 0".351 $\pm$ 0".069, for the low redshift sample. The corresponding velocity dispersions are 186 $\pm$ 21 km s^{-1}, and 141 $\pm$ 28 km s^{-1}.

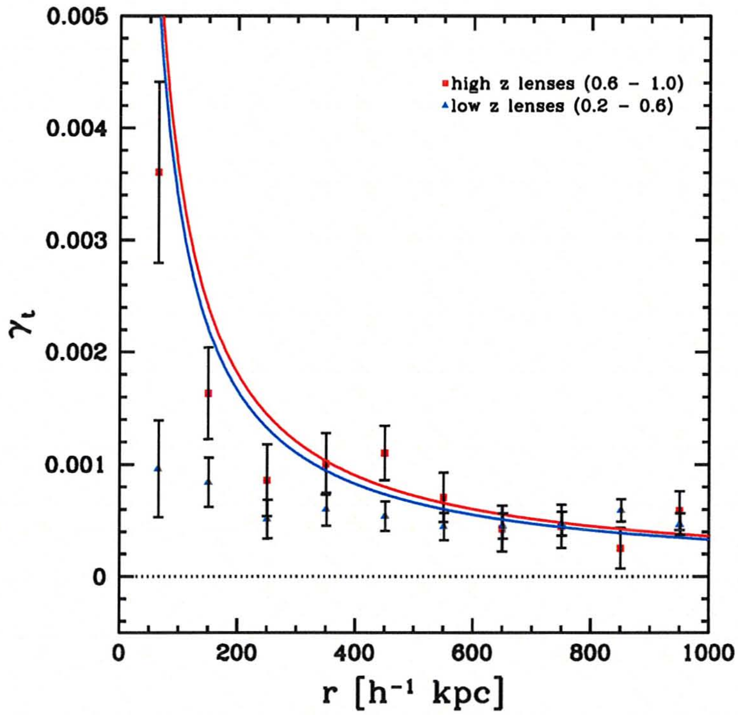

Figure 3.7 : The ensemble-averaged tangential shear as a function of physical distance for a sample of CFHTLS galaxies divided by redshift. The best-fit isothermal sphere, shown with the solid line, yields an Einstein radius of 0".140 $\pm$ 0".016, for the high redshift sample, and 0".189 $\pm$ 0".031, for the low redshift sample. The corresponding velocity dispersions are 105 $\pm$ 12 km s^{-1}, and 100 $\pm$ 16 km s^{-1}.

Sample	$\langle z \rangle$	$\langle \beta \rangle$	$\langle L \rangle$ $10^9 h^{-2} L_{\odot B}$	$\langle \sigma \rangle$ km s^{-1}	α	σ_* km s^{-1}	L_* $10^{10} h^{-2} L_{\odot B}$	M_{*total} $10^{12} h^{-1} M_\odot$	M_{total} $10^{12} h^{-1} M_\odot$	M_*/L_* $hM_\odot/L_{\odot B}$	M/L $hM_\odot/L_{\odot B}$
Full	0.54	0.55	4.79	85 ± 7	3	113 ± 9	1.124	1.7 ± 0.3	0.98 ± 0.18	154 ± 28	204 ± 37
Full	0.54	0.55	4.79	85 ± 7	4	105 ± 9	1.124	1.5 ± 0.3	0.98 ± 0.18	133 ± 24	204 ± 37
Full (kpc)	0.45	0.60	3.07	98 ± 13	3	151 ± 21	1.124	3.1 ± 0.7	1.3 ± 0.3	275 ± 58	423 ± 90
Full (kpc)	0.45	0.60	3.07	98 ± 13	4	136 ± 18	1.124	2.5 ± 0.5	1.3 ± 0.3	221 ± 47	423 ± 90
Bright	0.68	0.48	72.18	154 ± 8	3	-	-	-	3.2 ± 0.5	-	45 ± 8
Bright	0.68	0.48	72.18	154 ± 8	4	-	-	-	3.2 ± 0.5	-	45 ± 8
Intermediate	0.65	0.50	11.47	105 ± 10	3	-	-	-	1.5 ± 0.3	-	130 ± 24
Intermediate	0.65	0.50	11.47	105 ± 10	4	-	-	-	1.5 ± 0.3	-	130 ± 24
Faint	0.41	0.62	1.29	47 ± 9	3	-	-	-	0.30 ± 0.60	-	231 ± 46
Faint	0.41	0.62	1.29	47 ± 9	4	-	-	-	0.30 ± 0.60	-	231 ± 46
Red	0.58	0.53	16.13	159 ± 18	3	141 ± 16	1.124	2.7 ± 0.5	3.4 ± 0.7	238 ± 47	211 ± 42
Red	0.58	0.53	16.13	159 ± 18	4	145 ± 17	1.124	2.8 ± 0.6	3.4 ± 0.7	253 ± 50	211 ± 42
Green	0.50	0.57	7.20	93 ± 9	3	107 ± 11	1.124	1.6 ± 0.3	1.2 ± 0.2	139 ± 26	161 ± 31
Green	0.50	0.57	7.20	93 ± 9	4	104 ± 10	1.124	1.4 ± 0.3	1.2 ± 0.2	129 ± 25	161 ± 31
Blue	0.55	0.55	3.88	71 ± 8	3	102 ± 12	1.124	1.4 ± 0.3	0.69 ± 0.14	124 ± 25	177 ± 35
Blue	0.55	0.55	3.88	71 ± 8	4	93 ± 11	1.124	1.2 ± 0.2	0.69 ± 0.14	104 ± 21	177 ± 35
$0.2 < z < 0.6$	0.39	0.63	2.71	73 ± 6	3	106 ± 9	0.8219	1.5 ± 0.3	0.73 ± 0.13	186 ± 34	269 ± 49
$0.2 < z < 0.6$	0.39	0.63	2.71	73 ± 6	4	97 ± 8	0.8219	1.3 ± 0.2	0.73 ± 0.13	155 ± 28	269 ± 49
$0.2 < z < 0.6$ (kpc)	0.35	0.65	2.11	100 ± 16	3	158 ± 26	0.8219	3.4 ± 0.8	1.4 ± 0.3	410 ± 95	645 ± 149
$0.2 < z < 0.6$ (kpc)	0.35	0.65	2.11	100 ± 16	4	141 ± 23	0.8219	2.7 ± 0.6	1.4 ± 0.3	327 ± 75	645 ± 149
$0.6 < z < 1.0$	0.78	0.44	11.42	106 ± 13	3	107 ± 13	1.177	1.5 ± 0.3	1.5 ± 0.3	131 ± 26	133 ± 27
$0.6 < z < 1.0$	0.78	0.44	11.42	106 ± 13	4	107 ± 13	1.177	1.5 ± 0.3	1.5 ± 0.3	131 ± 26	133 ± 27
$0.6 < z < 1.0$ (kpc)	0.76	0.44	11.96	105 ± 12	3	107 ± 13	1.177	1.6 ± 0.3	1.5 ± 0.3	132 ± 27	136 ± 27
$0.6 < z < 1.0$ (kpc)	0.76	0.44	11.96	105 ± 12	4	107 ± 13	1.177	1.5 ± 0.3	1.5 ± 0.3	131 ± 26	136 ± 27

Table 3.2 Properties of all of the lens samples calculated using 2 different scaling laws. Where noted, the sample was calculated in physical units (kpc) not angular ones. The quoted errors do not include mass model uncertainties.

3.4 Halo Shapes

Introduction

One important feature of dark matter halos is their shape. It is known that the projected shapes of galaxies on the sky are elliptical in nature, but the shapes of their dark matter halos could be oblate, prolate or triaxial. Observationally, measuring the shapes of dark matter halos is difficult. This is because of the large amounts of data required to make a significant measurement (weak lensing), or because of the lack of visible tracers available (dynamical measurements). Comparing results from numerical simulations to observations is an important constraint on CDM models. Weak lensing has the possibilty of making this measurement. Thus far, most dynamical, kinematic and lensing measurements have assumed spherical halos. Numerical simulations of CDM show indications that dark matter halos should be flattened, with a slight preference for prolateness over oblateness (Dubinski & Carleberg, 1991; Springel et al., 2004; Allgood et al., 2006; Bett et al., 2007). Spherical halos tend to be produced in simulations of self-interacting dark matter (Davé et al., 2001).

Generally, galaxy-galaxy lensing measurements assume dark matter halos are spherical, but recent galaxy-galaxy measurements by Hoekstra et al. (2004) and Parker et al. (2007) detect flattening of dark matter halos at $> 2\sigma$ significance. These results are not seen in the SDSS data analysis by Mandelbaum et al. (2006b). However, when restricted to a sample of red galaxies, Mandelbaum et al. did find marginal evidence for flattened halos.

It should be noted that these measurements rely on assumptions about the alignment of the ellipticity of the light distribution and the mass distribution. If the halo flattening is not correlated with the orientation of the light profile, this measurement is more difficult to interpret, and any detected flattening signal is likely systematically supressed. Using the CFHTLS data set presented here, we decided to test for halo flattening for our entire sample, as well as samples divided by colour.

Brainerd & Wright (2000) have suggested a simple way to mesaure halo shapes from weak lensing measurements. They suggest comparing the tangential shear from sources close to the minor axes versus the major axes (see Figure 3.8) and looking for differences in the signal from the two regions. Any difference in signal between the two regions can be used to estimate the flattening of galaxy dark matter halos. This technique has been used by Parker et al. (2007), who found that halos on average have an ellipticity of ~ 0.3 with a $\sim 2\sigma$ detection.

The analysis described in the previous sections was repeated for the entire sample of lenses, as well as the red, green, blue and a sample of bright red ($M_{r'} <$ -21.5) lenses. This time the sources were divided into those within 45 degrees of the semi-major axis and those within 45 degrees of the semi-minor axis (see the schematic in Figure 3.8). The tangential shear results can be seen in Figures 3.9 - 3.13. The signal from the two angular bins of sources for the entire sample of lenses is distinct. The best fit isothermal sphere for sources within 45° of the semi-major axis and for sources within 45° of the semi-minor axis yield Einstein radii of 0".161 $\pm$ 0".019 and 0".067 $\pm$ 0".008.

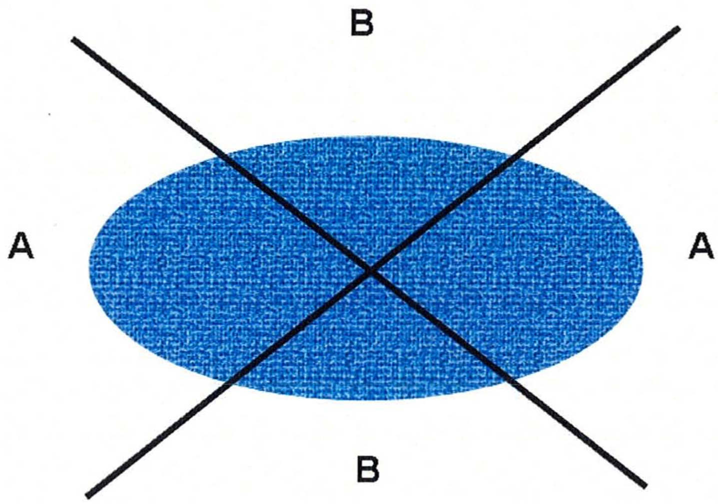

Figure 3.8 : Schematic of Anisotropic Shear. If galaxy halos are not spherical, there should be a difference in the weak lensing signal from regions labeled with an A versus those labeled with a B.

These correspond to velocity dispersions of 101 $\pm$ 12 km s^{-1} and 65 $\pm$ 8 km s^{-1}.

Following the method of Brainerd & Wright, we calculated the ratio of $\langle\gamma\rangle_{minor}$ to $\langle\gamma\rangle_{major}$. The results for the entire sample of lenses can be seen in Figure 3.9 (*left*) and the best fit value was 0.43 $\pm$ 0.11 indicating a $> 5\sigma$ detection of non-spherical dark matter halos. Our best fit shear ratio indicates a halo ellipticity of 0.70 $\pm$ 0.18 (see Figure 3.9 (*right*)). Our finding indicates that galaxy dark matter halos are more elliptical in projection than the light distribution of the galaxies. If we restrict our measurement of the shear signal to within 45 arcseconds (to better match the simulations of Brainerd & Wright) we find $\langle\gamma\rangle_{minor}/\langle\gamma\rangle_{major} = 0.57 \pm 0.15$ favouring a halo with an ellipticity of 0.52 $\pm$ 0.13. Both measurements indicate a flattened dark matter halo at $>\sim 3\sigma$. We also computed this ratio within 90 arcseconds and 120 arcseconds as can be seen in Figure 3.14. The difference that can be seen by probing different distances of the halo when making shape measurements indicates a need for further study of the distances to which these measurements should be made to be considered a valid measure of halo shape.

An alternative method to measuring halo ellipticity by using binned measurements (which are sensitive to bin size) would be to calculate the ratio of $\langle\gamma\rangle_{minor}$ to $\langle\gamma\rangle_{major}$ inside some distance. We have also calculated the ratio inside 1 arcminute and 2 arcminutes. For the entire sample this yielded results of $\langle\gamma\rangle_{minor}/\langle\gamma\rangle_{major} = 0.57 \pm 0.15$ and $< e > = 0.52 \pm 0.14$ inside 1 arcminute and $\langle\gamma\rangle_{minor}/\langle\gamma\rangle_{major} = 0.42 \pm 0.10$ and $< e > = 0.70 \pm 0.16$ inside 2 arcminutes. These measurements can be seen in Table 3.3.

It is important to measure the anisotropic lensing signal for a sample of well known lenses. One way to improve this anisotropic weak lensing measurement would be to select a sample of lenses with a well defined semi-major axis direction. This would mean either selecting only brighter lenses, or removing galaxies with noisy shape measurements or with low ellipticity. For a lens with a low measured ellipticity, determining the semi-major axis accurately is difficult and error prone.

Also of interest is to divide the lens population into red, blue and in our case green subsamples using colour information. We used the colour samples defined earlier as well as a bright red sample. Our red galaxies yield a shear ratio of 0.43 ± 0.10 favouring a halo with an ellipticity of 0.70 ± 0.17, which is consistent with our entire lens sample detection. Our bright red galaxies yield similar results as the red galaxies. The green sample of galaxies shows no detection for a non-spherical halo. Most surprising was the results for the blue sample of galaxies. The blue galaxies yield a shear ratio of 0.23 ± 0.16 favouring a halo with an ellipticity of 0.88 ± 0.52. While this result is indicating a high ellipticity for blue galaxy halos, some caution needs to be exerted in its interpretation. Previous studies of dark matter halos of spiral galaxies have yielded conflicting results. A study by Navarro et al. (2004) indicated that on small scales the disk spin axis is aligned with the minor axis of the dark matter halo, but on larger scales the disk is aligned with the halo. In contrast, N-body simulations of satellite distributions with the observed satellite distribution for the Milky Way suggest that the disk is aligned with the major-axis of the halo (e.g. Zentner et al., 2005).

We also made the measurements inside 1 arcminute and 2 arcminutes for the colour selected lenses and to remove any galaxies that may have poorly measured ellipticities, we also divided our sample into bright and faint lenses, and a bright sample of blue galaxies. The results can be seen in Table 3.3. Even after removing any galaxies that may have had poorly measured ellipticities, the bright blue sample still shows a detection for non-spherical dark matter halos. By using more data, or combining the CFHTLS wide and deep field components this measurement can be improved further and the precision increased, and we will be able to better estimate the ellipticity of dark matter halos.

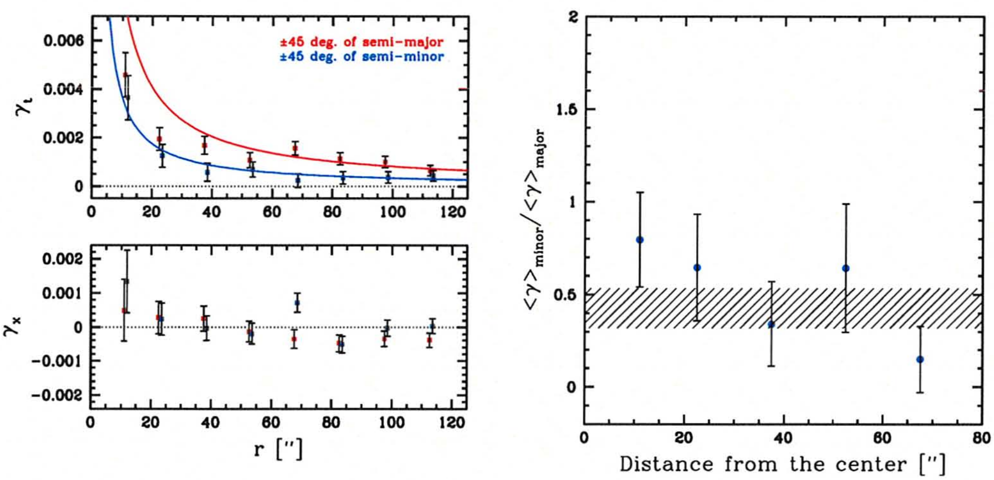

Figure 3.9 (*Left top*): Mean tangential shear for sources close to the semi-major axis (red) and close to the semi-minor axis (blue). The best fit isothermal sphere for sources within 45° of the semi-major axis yields an Einstein radius of 0".161 ± 0".019 corresponding to a velocity dispersion of 101 ± 12 km s^{-1}. The best fit isothermal sphere for sources within 45° of the semi-minor axis yields an Einstein radius of 0".067 ± 0".008 corresponding to a velocity dispersion of 65 ± 8 km s^{-1}. (*Left bottom*): The cross-shear signal when the source images are rotated by 45°. (*Right*): Ratio of mean shear experienced by sources closest to the minor axis of an elliptical lens to those experienced by sources closest to the major axis. The weighted average shear ratio is 0.43 ± 0.11 favouring a halo with an ellipticity of 0.70 ± 0.18. The shaded region indicates the 1σ error on the weighted average ratio.

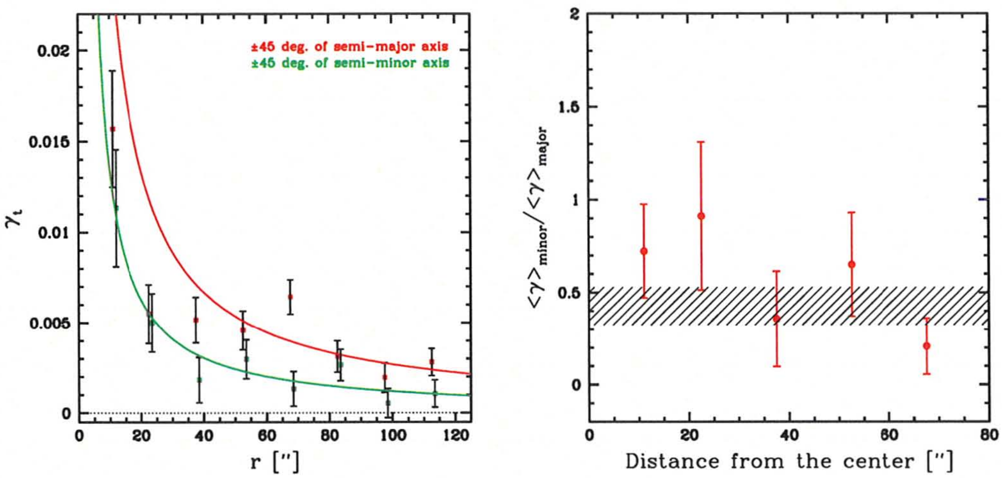

Figure 3.10 (*Left*): Mean tangential shear for sources close to the semi-major axis (red) and close to the semi-minor axis (green), for red lenses as defined in Figure 2.5. The best fit isothermal sphere for sources within 45° of the semi-major axis yields an Einstein radius of 0".535 $\pm$ 0".077 corresponding to a velocity dispersion of 187 $\pm$ 27 km s^{-1}. The best fit isothermal sphere for sources within 45° of the semi-minor axis yields an Einstein radius of 0".238 $\pm$ 0".040 corresponding to a velocity dispersion of 125 $\pm$ 21 km s^{-1}. (*Right*): Ratio of mean shear experienced by sources closest to the minor axis of an elliptical lens to those experienced by sources closest to the major axis. The weighted average shear ratio is 0.43 $\pm$ 0.10 favouring a halo with an ellipticity of 0.70 $\pm$ 0.17. The shaded region indicates the 1σ error on the weighted average ratio.

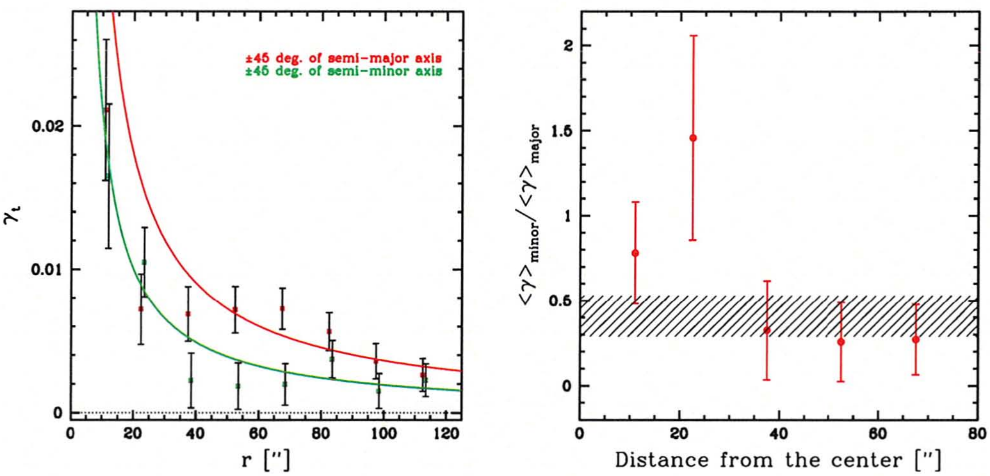

Figure 3.11 (*Left*): Mean tangential shear for sources close to the semi-major axis (red) and close to the semi-minor axis (green), for red lenses as defined in Figure 2.5 with $M_{r'}$ < -21.5. The best fit isothermal sphere for sources within 45° of the semi-major axis yields an Einstein radius of 0".724 ± 0".090 corresponding to a velocity dispersion of 225 ± 28 km s^{-1}. The best fit isothermal sphere for sources within 45° of the semi-minor axis yields an Einstein radius of 0".383 ± 0".061 corresponding to a velocity dispersion of 164 ± 26 km s^{-1}. (*Right*): Ratio of mean shear experienced by sources closest to the minor axis of an elliptical lens to those experienced by sources closest to the major axis. The weighted average shear ratio is 0.41 ± 0.12 favouring a halo with an ellipticity of 0.72 ± 0.21. The shaded region indicates the 1σ error on the weighted average ratio.

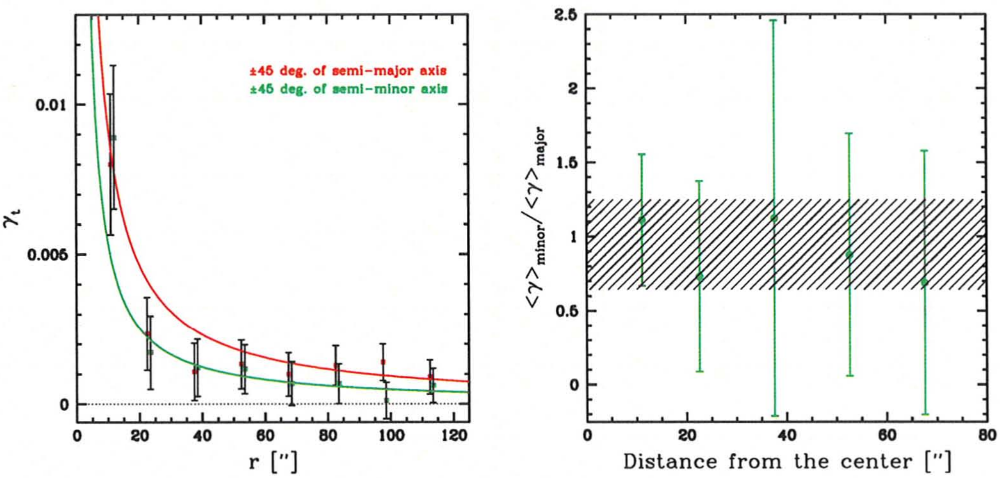

Figure 3.12 (*Left*): Mean tangential shear for sources close to the semi-major axis (red) and close to the semi-minor axis (green), for green lenses as defined in Figure 2.5. The best fit isothermal sphere for sources within 45° of the semi-major axis yields an Einstein radius of 0".185 ± 0".025 corresponding to a velocity dispersion of 106 ± 14 km s^{-1}. The best fit isothermal sphere for sources within 45° of the semi-minor axis yields an Einstein radius of 0".096 ± 0".0.020 corresponding to a velocity dispersion of 76 ± 16 km s^{-1}. (*Right*): Ratio of mean shear experienced by sources closest to the minor axis of an elliptical lens to those experienced by sources closest to the major axis. The weighted average shear ratio is 0.95 ± 0.30 favouring a halo with an ellipticity of 0.07 ± 0.02. The shaded region indicates the 1σ error on the weighted average ratio.

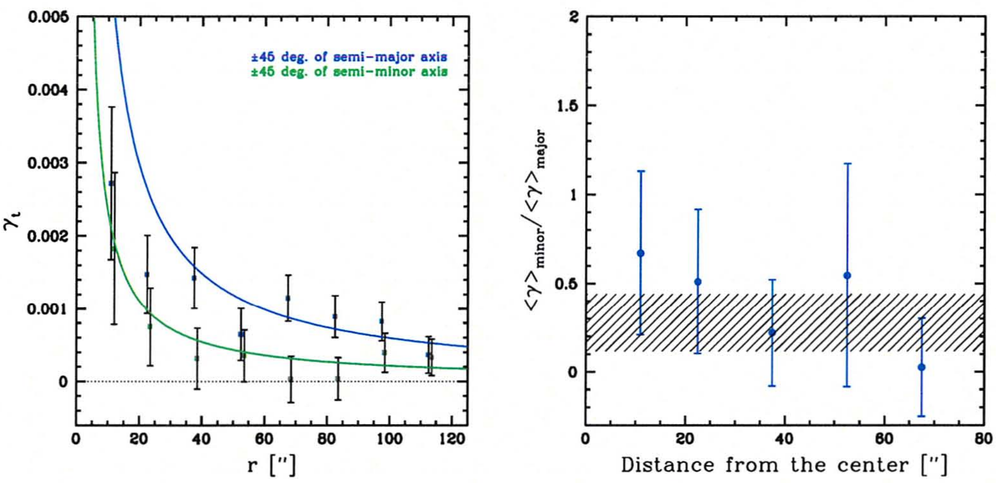

Figure 3.13 (*Left*): Mean tangential shear for sources close to the semi-major axis (blue) and close to the semi-minor axis (green), for blue lenses as defined in Figure 2.5. The best fit isothermal sphere for sources within 45° of the semi-major axis yields an Einstein radius of 0".119 ± 0".017 corresponding to a velocity dispersion of 87 ± 12 km s^{-1}. The best fit isothermal sphere for sources within 45° of the semi-minor axis yields an Einstein radius of 0".042 ± 0".011 corresponding to a velocity dispersion of 52 ± 13 km s^{-1}. (*Right*): Ratio of mean shear experienced by sources closest to the minor axis of an elliptical lens to those experienced by sources closest to the major axis. The weighted average shear ratio is 0.23 ± 0.16 favouring a halo with an ellipticity of 0.88 ± 0.52. The shaded region indicates the 1σ error on the weighted average ratio.

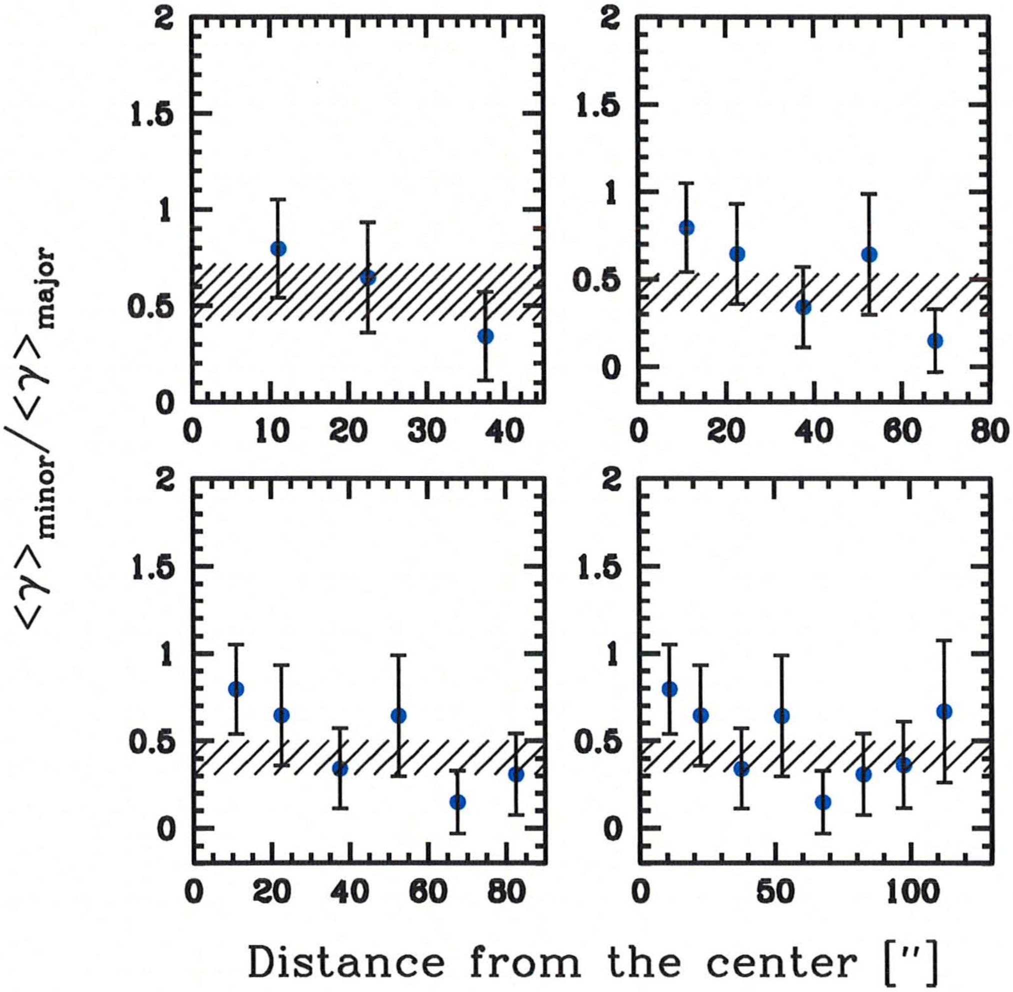

Figure 3.14 Ratio of mean shear experienced by sources closest to the minor axis of an elliptical lens to those experienced by sources closest to the major axis for the entire lens sample measured for 4 different angular distances from the center of the lens. The shaded regions indicate the 1σ error on the weighted average ratio for each sample. (*Upper Left*): Ratio of mean shear inside 45". The weighted average shear ratio is 0.57 ± 0.15 favouring a halo with an ellipticity of 0.52 ± 0.13. (*Upper Right*): Ratio of mean shear inside 80" (see Figure 3.9). The weighted average shear ratio is 0.43 ± 0.11 favouring a halo with an ellipticity of 0.70 ± 0.18. (*Lower Left*): Ratio of mean shear inside 90". The weighted average shear ratio is 0.41 ± 0.10 favouring a halo with an ellipticity of 0.72 ± 0.17. (*Lower Right*): Ratio of mean shear inside 120". The weighted average shear ratio is 0.41 ± 0.09 favouring a halo with an ellipticity of 0.71 ± 0.15.

Sample	$\gamma_{min}/\gamma_{maj}$ (< 1')	$< e >$ (< 1')	$\gamma_{min}/\gamma_{maj}$ (< 2')	$< e >$ (< 2')
Full	0.57 ± 0.15	0.52 ± 0.14	0.42 ± 0.10	0.70 ± 0.16
Red	0.62 ± 0.15	0.46 ± 0.11	0.48 ± 0.10	0.63 ± 0.14
Bright Red	0.56 ± 0.19	0.54 ± 0.15	0.54 ± 0.12	0.56 ± 0.12
Green	0.94 ± 0.41	0.08 ± 0.03	0.62 ± 0.25	0.47 ± 0.19
Blue	0.43 ± 0.22	0.70 ± 0.36	0.34 ± 0.15	0.80 ± 0.35
Full Bright ($M_{r'}$ < -20)	0.60 ± 0.15	0.48 ± 0.12	0.42 ± 0.10	0.70 ± 0.16
Full Faint ($M_{r'}$ > -20)	0.52 ± 0.27	0.58 ± 0.31	0.42 ± 0.19	0.71 ± 0.31
Bright Blue ($M_{r'}$ < -19)	0.44 ± 0.21	0.68 ± 0.32	0.39 ± 0.14	0.74 ± 0.27

Table 3.3 Anisotropic tangential shear ratios and halo ellipticities calculated for within 1' and 2' of the host lens. Errors quoted in the ellipticities are a lower limit propagated from the errors in the tangential shear ratios.

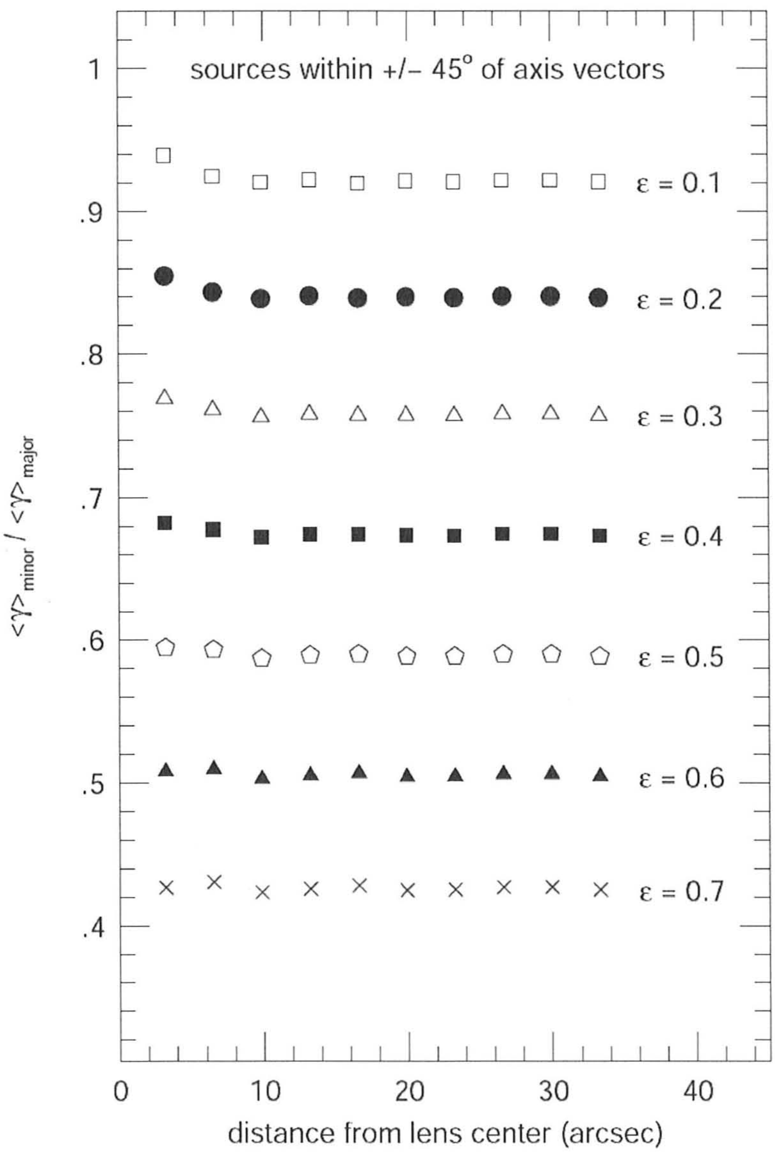

Figure 3.15 Ratio of mean shear expected by sources closest to the minor axis of an elliptical lens to those experienced by sources closest to the major axis for model data. Figure from Brainerd and Wright (2000).

Chapter 4

Discussion & Conclusions

4.1 Results & Interpretation

We have used data in u*,g',r',i', and z' from the T0003 release of the CFHTLS-Deep to detect a significant galaxy-galaxy lensing signal in multiple samples. Our main results and interpretations are as follows:

• We measured a weak lensing signal for our entire lens sample in both angular and physical units. It is significant at $> 12\sigma$ when measured in angular units and at $> 7\sigma$ when measured in physical units. The measured velocity dispersion for an L_* galaxy is 113 ± 9 kms^{-1} and 151 ± 21 kms^{-1} for the samples measured in angular and physical units, respectively. The isothermal sphere model used here fit much better for the angular bins than the physical ones. We also estimated the total mass of an L_* galaxy at a redshift of 0.54 to be $1.7 \pm 0.3 \times 10^{12}$ h^{-1}M$_\odot$.

• We divided our lenses into 3 different luminosity samples and detected a clear difference between them. The measured velocity dispersions were 154 ±

8 kms^{-1}, 105 $\pm$ 10 kms^{-1}, and 47 $\pm$ 9 kms^{-1} for the bright, intermediate and faint luminosity samples, respectively. These samples were used to create a B-band Tully-Fisher relation and the slope measured agrees with theoretical predictions from the virial theorem.

- In an attempt to search for galaxy halo evolution, we divided our lenses into a high and low redshift sample using both angular and physical units. There was a difference in the tangential shear profiles for the two sub-samples when computed in angular units, but when the velocity dispersions were scaled to a typical L_* galaxy, we found no conclusive evidence for evolution in galaxy dark matter halos.

The differences seen in the average redshift and luminosities for the samples calculated in angular versus physical units can possibly be attributed to the fact that the same scales are not being probed. For the sample computed in angular units, we calculated the tangential shear inside 2 arcminutes, whereas for the sample in physical units, we probed out to 1 h^{-1}Mpc. At a redshift of 0.3 for example, 2 arcminutes corresponds to $\sim$ 374 h^{-1}kpc for our adopted cosmology, which is $\sim$ 1/3 of the distance we probed in physical units. The other issue is that the bin sizes for these two samples were not identical. The size of the bins used, and the distances probed for making these measurements, and even whether angular or physical units are used make a significant difference for the signal computed. This indicates a need for caution when interpreting results for halo evolution since they are very sensitive to the scales used.

- We measured the shapes of galaxy dark matter halos for our entire lens sample and found conclusive evidence for non-spherical dark matter halos in agreement with ΛCDM predictions (Dubinski & Carleberg, 1991). We also subdivided our lenses by colour and significant detections for flattened halos were seen in our red and blue, but not green sub-samples. Regardless of whether the shape measurement was computed using bins (which are sensitive to bin size) and an isothermal sphere fit, or determining the mean shear shape inside a given radius, a clear detection for non-spherical dark matter halos was found. This is the first conclusive measurement of non-spherical dark matter halos to date.

As can be seen in Figure 3.14, the radial extent of the galaxy-galaxy lensing measurement matters. One method that can get around this "extent" issue is using the maximum-likelihood method proposed by Schneider & Rix (1997), and implemented by Kleinheinrich et al. (2006). With this method, one assumes a specific halo lens model, and then computes the shear γ_{ij} on each source j from each lens i. As several halos may contribute to the shear of a given source, the shear contributions from different lenses are summed together to determine the total shear acting on source j. Using the shear and observed PSF corrected ellipticity, the intrinsic ellipticity can be estimated. The probability of observing a given intrinsic ellipticity is calculated, and then by multiplying the probabilities from all sources, one determines the likelihood for a given set of parameters of the lens model. With this approach, the model with the highest likelihood is the one that produces shear-corrected source orientations that are oriented isotropically. The advantage of this method is that it can fit for the extent of the dark matter halo and for the velocity dispersion

σ simultaneously, without having to make any assumptions. Our method of stacking the shear signal around foreground lenses is more direct, but cannot be used to determine the extent of dark matter halos.

4.2 Comparison to other work

Entire Sample

The measured velocity dispersion for our L_* galaxy is 113 $\pm$ 9 kms^{-1}. This is slightly lower than previous results (Parker et al., 2007; Kleinheinrich et al., 2006; Hoekstra et al., 2004) but agrees within 2σ. The estimated total mass for our L_* galaxy, $M_{*total} = 1.7 \pm 0.3 \times 10^{12}\ h^{-1}M_{\odot}$, is in good agreement with the CFHTLS results of Parker et al, 2007, and COMBO-17 results of Kleinheinrich et al., 2006.

Colour and Luminosity Samples

The best survey to date for comparing weak lensing measurements is the Sloan Digital Sky Survey (SDSS). This is a shallow but wide survey, where spectroscopic redshifts are available for the lenses and photometric redshifts for the sources. Recently, Mandelbaum et al. (2006a), divided their lens sample into luminosity bins and then subdivided them into early- and late-type galaxies using morphology information. Unfortunately, these results are very difficult to compare with ours as the lensing measurements were made for halos of central galaxies, and not for the individual "isolated" galaxies studied here. With SDSS spectroscopy, Mandelbaum et al. (2006a) identified central galaxies as distinct from satellites. The model used for computing the central halo masses is outlined in Mandelbaum et al. 2005.

The velocity dispersion and mass for an L_* galaxy for our colour selected sample are: $\sigma_* = 1 \pm 1$ and $M_{*total} = 2.7 \pm 0.5 \times 10^{12}\ h^{-1}M_\odot$ for the red sample, $\sigma_* = 107 \pm 11$ and $M_{*total} = 1.6 \pm 0.3 \times 10^{12}\ h^{-1}M_\odot$ for the green sample, and $\sigma_* = 102 \pm 12$ and $M_{*total} = 1.4 \pm 0.3 \times 10^{12}\ h^{-1}M_\odot$ for the blue sample. These results are consistent within 1σ errrors to the results of Kleinheinrich et al. (2006). While the results are consistent, it should be noted that their sample was divided into 2 colour bins and not 3, and that they computed the mass within a smaller physical scale than we did.

For our luminosity sample, there is an agreement with the observed trend that with increasing luminosity there is an increase in mass as seen by Hoekstra et al. (2005). A detailed comparison is not possible because of differences in the range of luminosities studied and the fact that an NFW profile was used instead of a singular isothermal sphere.

Evolution

We found no evidence for evolution in galaxy dark matter halos confirming previous measurements. Previous studies by Parker et al., (2007) using apparent i' magnitudes to select a high and low redshift sample, and Wilson et al., (2001) using bright early-type galaxies, did not detect any evolution in galaxy dark matter halos.

Halo Shapes

Recent galaxy-galaxy lensing measurements by Hoekstra et al. (2004) using RCS data detected a flattening of dark matter halos at the 2 - 3σ level. Parker et al. (2007) found some evidence for non-spherical dark matter halos using the same methods implemented here on the CFHTLS-Wide data. SDSS results of Mandelbaum et al. (2006b) indicated no observed flattening, however, if they restricted their lens sample to red galaxies, a marginal detection of flattening was seen. We have made the first conclusive detection of non-spherical galaxy dark matter halos, in agreement with the predictions of CDM (Dubinski & Carleberg, 1991). Alternative theories of gravity, such as Modified Newtonian Dynamics (MOND) (Milgrom, 2002), predict that 'halos' should appear spherical on these scales, in direct contradiction with our results.

4.3 Looking Forward

4.3.1 How to improve these measurements

Galaxy-galaxy lensing is a powerful tool for studying the properties of dark matter halos of galaxies out to large distances. While this technique has been used many times to learn more about dark matter halos, the measurements can still be improved. We presented results of the shape measurements of galaxy halos, but using a sample of truly isolated galaxies to make this measurement would be a further improvement. A survey with good local density measurements would allow one to find isolated galaxies and thus enable better galaxy halo shape measurements, free from possible contamination due to nearby neighbours.

In our study of galaxy-galaxy lensing using CFHTLS-Deep data, we had photometric redshifts available, and many bands allowed us to divide our lens sample in several interesting ways. Other things we would like to know which would aid in studies of galaxy dark matter halos are the physical morphologies of the galaxies and their stellar masses. Currently, using WIRCAM on the CFHT, near-IR data for some of the Deep fields are being obtained. Near-IR data can improve our photometric redshifts and improve the spectral energy distribution (SED) fits for determining stellar masses.

We can also improve our data set by combining the WIDE and DEEP fields from the CFHTLS. By having more galaxies, we can improve our uncertainties, and perhaps increase the significance of our detections for halo flattening, luminosity and colour measurements. It would also allow for further study of halo evolution by having a larger sample of galaxies, which would allow for smaller redshift slices to be made.

We have discussed the difficulties that can arise when determining what bin sizes to use and the radial extent to probe when trying to determine information about galaxy dark matter halos. By comparing to simulations, we could get a better understanding of the optimal extent that we should probe when making measurements of dark matter halos. We could also use bins that have equal signal-to-noise (S/N) per bin to try to remove any bias that may come in when choosing bin sizes.

4.3.2 Future Projects

Weak gravitational lensing has an exciting future. There are currently surveys in progress and many ground- and space-based surveys that are planned. In lensing surveys, the strategy is to image large fields with very high image quality, which then creates a vast amount of data that can be used for many scientific purposes. Many of the current and proposed weak lensing surveys are scientifically driven by the desire for measurements of cosmic shear and the estimation of cosmological parameters, but the data have legacy value for other extra-galactic projects.

As more data are becoming available for weak lensing studies, the understanding of systematic errors becomes more important. Previously, statistical errors were significant for weak lensing measurements, but from the CFHTLS-Deep results presented here, we see that statistical errors are now quite small. Currently, the limitations for both galaxy-galaxy and cosmic shear measurements are accurately (in an unbiased way) measuring shapes and determining source redshifts. The source redshift distribution needs to be well understood to be able to convert measured shear signals to physical quantities such as mass (galaxy-galaxy lensing), or cosmological parameters (cosmic shear). Ideally spectroscopic redshifts would be used, but this is unrealistic for surveys of this size with such faint sources.

If we can escape the atmosphere and observe in space, we can minimize many systematic errors. Space-based images have a larger number of sources for a given magnitude limit that can be resolved better than ground-based observations. Unfortunately, space-based observations are costly and are typically limited to small fields. Currently, there is a proposed space observatory called the SuperNova Acceleration Probe (SNAP) designed to measure the expansion of the Universe and to learn more about Dark Energy.[1] It is proposed as part of the Joint Dark Energy Mission (JDEM) which would launch around 2015.[2] It would comprise a ~ 2 metre telescope capable of imaging in both the optical and infrared, designed for learning more about dark energy through cosmic shear and type Ia supernovae studies. While JDEM has a goal of measuring the dark energy equation of state and its evolution, the data would also be useful for galaxy-galaxy lensing measurements. With high resolution images, shape measurements can be made very accurately, and detailed lens morphologies could be calculated. These data would be well suited for weak lensing studies of galaxies as a function of their observed properties and their evolution, a complement to the CFHTLS-Deep study carried out here.

While imaging surveys from space will provide a lot of data for weak lensing studies, there are also many ambitious ground-based projects planned. While the CFHTLS data will be very useful for weak lensing studies for some time, the next generation of surveys will start in ~ 2010 in both the optical and infrared using Omegacam on the Very Large Telescope Survey Telescope (VST) (optical) and the Visible and Infrared Survey Telescope for Astronomy (VISTA) (infrared).[3,4] Both VISTA and the VST will image ~ 1500 square degrees of the sky with the goals of accurate photometric redshifts (VISTA) and studying weak gravitational lensing. Other new projects include the addition of the HyperSuprime Cam on Subaru which is set to see first light in 2011.

[1] http://snap.lbl.gov/

[2] http://jdem.gsfc.nasa.gov/

[3] http://www.eso.org/sci/observing/policies/PublicSurveys/sciencePublicSurveys.html#VST

[4] http://www.vista.ac.uk/

This new camera will allow for studies of weak lensing and galaxy evolution with image quality $< 0.4''$.[5] Pan-STARRS, a panoramic survey telescope and rapid response system, while primarily intended for detecting potentially hazardous objects in our Solar System, will be quite useful for studies of galaxies and cosmology including weak lensing studies of cosmic shear.[6] When completed, Pan-STARRS will be capable of imaging $\sim 30{,}000$ square degrees of sky, covering ~ 6000 square degrees per night to a depth of $\sim 24^{th}$ magnitude. Pan-STARRS, led by the University of Hawaii already has a prototype completed.

Looking to the longer term, in development is a new camera for the Dark Energy Survey (DES). [7] A 3 square degree camera set to image ~ 5000 square degrees of the sky in 4 filters to study dark energy using cluster counts, weak lensing, supernovae and baryon acoustic oscillations, using the 4 metre Blanco telescope at CTIO. Finally, set to have first light in 2014, the Large Synoptic Survey Telescope (LSST) will image 30,000 square degrees of the sky with a larger collecting area than Pan-STARRS, using a 8.4 metre telescope with a 9.6 degree^2 field-of-view.[8] Using 6 bands, the LSST aims to study transient objects and to map the Milky Way, as well as to study dark matter and dark energy. The deep multiband data that will be available will be ideal for photometric redshift determination and lensing measurements.

This thesis has provided an insight into some of what has been and can be done using weak lensing on galaxy scales. There are still many unanswered

[5] http://www.astro.princeton.edu/ ~rhl/HSC/hscsurvey2.pdf

[6] http://pan-starrs.ifa.hawaii.edu/public/science-goals/science-goals.html

[7] http://www.darkenergysurvey.org/

[8] www.lsst.org/

questions about galaxy formation and evolution, and much of this centers on a better understanding of the relationship between galaxies and their dark matter halos. Gravitational lensing, and especially weak gravitational lensing has, and will continue to play a large role in linking galaxies to their halos.

Bibliography

Agustsson, I. & Brainerd, T.G. 2006, ApJ, 644, L25

Alcock, C. et a,l. 2000, ApJ, 542, 281

Allgood, B. et al. 2006, MNRAS, 367, 1781

Angloher, G. et al. 2009, APh, 31, 270

Bacon, D.J., Refregier, A.R. & Ellis, R.S. 2000, MNRAS, 318, 625

Bartelmann, M. & Schneider, P. 2001, Physics Reports, 340, 291

Beckwith, S.V.W. et al. 2006, AJ, 132, 1729

Bernstein, G.M,, & Jarvis, M. 2002, AJ, 123, 583

Bernstein, G.M., & Norberg, P. 2002, AJ, 124, 733

Bett, P. et al. 2007, MNRAS, 376, 215

Brainerd, T., Blanford, R. & Smail, I. 1996, ApJ, 466, 623,

Brainerd, T., Blandford, R., & Smail, I. 1996, ApJ, 466, 623

Brainerd, T., & Wright, C.O. 2000, *e-print arXiv:astro-ph/0006281*

Combes, F. 2004, *e-print arXiv:astro-ph/0309755*

Clowe, D. et al. 2006, ApJ, 648, L109

Davé, R., Spergel, D.N., Steinhardt, P.J., & Wandelt, B.D. 2001, ApJ, 547, 574

De Rijcke, S. et al. 2007, ApJ, 659, 1172

Dubinski, J. & Carleberg, R.G. 1991, ApJ, 378, 496

Duc, P., Bournaud, F., & Brinks, E. 2008, *e-print arXiv:0707.3991*

Eggen, O.J.ynden-Bell, D., Sandage, A.R. 1962, ApJ, 136, 748

Faber, S.M. & Jackson, R.E. 1976, ApJ, 204, 668

Frei, Z. & Gunn, J.E., 1994, AJ, 108, 1476

Fukuda, Y. et al. 1998, Physical Review Letters, 81, 1562

Fukushige, T. & Makino, J. 1997, ApJ, 477, L9

Hoekstra, H., Franx, M., Kuijken, K. & Squires, G. 1998, ApJ, 504, 636

Hoekstra, H., Franx, M., & Kuijken, K. 2000, ApJ, 532, 88

Hoekstra, H., Franx, M., Kuijken, K., Carlberg, R.G., & Yee, H.K.C. 2003, MNRAS, 340, 609

Hoekstra, H., Yee, H.K.C., & Gladders, M.D. 2004, ApJ, 606, 67

Hudson, M.J., Gwyn, S.D.J., Dahle., H. & Kaiser, N. 1998, ApJ, 503, 531

Kaiser, N., & Squires, G. 1993, ApJ, 404, 441

Kaiser, N., Squires, G., & Broadhurst, T. 1995, 449, 460

Kaiser, N., Wilson, G., & Luppino, G.A. 2000, *e-print arXiv:astro-ph/0003338*

Kleinheinrich, M. et al. 2006, A&A, 455, 441

Klypin, A. 2000, *e-print arXiv:astro-ph/0005504*

Komatsu, E. et al., 2009, ApJS, 180, 330

Mandelbaum, R., Tasitsiomi, A., Seljak, U., Kravtsov, A.V., & Wechsler R.H., 2005, MNRAS, 362, 1451

Mandelbaum, R., Seljak, U., Kauffmann, G., Hirata, C.M., & Brinkmann, J. 2006a, MNRAS, 368, 715

Mandelbaum, R., Hirata, C.M., Broderick, T., Seljak, U., & Brinkmann, J. 2006b, MNRAS, 370, 1008

Mandelbaum, R., Seljak, U., Cool, R.J., Blanton, M., Hirata, C.M. & Brinkmann, J. 2006c, MNRAS, 372, 758

McKay, T.A. et al. 2001, *e-print arXiv:astro-ph/0108013*

Mellier, Y. 1999, ARA&A, 37, 127

Milgrom, M. 2002, New Astronomy Review, 46, 741

Minchin, R. et al., 2005, ApJ, 622, L21

Minchin, R. et al., 2007, ApJ, 670, 1056

Navarro, J.F., Frenk, C.S. & White, S.D. 1996, ApJ, 462, 563

Navarro, J.F., Abadi, M.G., Steinmetz, M. 2004, ApJ, 613, L41

Parker, L.C., Hudson, M.J., Carlberg, R., & Hoekstra, H. 2005, ApJ, 634, 806

Parker, L.C., Hoekstra, H., Hudson, M.J., van Waerbeke, L., & Mellier, Y. 2007, 669, 21

Peebles, P.J.E. 1965, ApJ, 142, 1317

Peebles, P.J.E. 1993, *Principles of Physical Cosmology*, Princeton University Press

Penny, S.J., Conselice, C.J., de Rijcke, S. & Held, E.V. 2009, MNRAS, 393, 1054

Perlmutter, S. et al. 1999, ApJ, 517, 565

Prada, F. et al. 2006, ApJ, 645, 1001

Press, W. H. & Schechter, P. 1974, ApJ, 187, 425

Riess, A.G. et al., 1998, AJ, 116, 1009

Rubin, V.C. & Ford, W.K. Jr. 1970, ApJ, 159, 379

Rubin, V. 1983, Science, 220, 1339

Rzepecki, J., Lombardi, M., Rosati, P., Bignamini, A., & Tozzi, P. 2007, A&A, 471, 743

Schneider, P., & Rix, H.-W. 1997, ApJ, 474, 25

Sheldon, E.S. et al. 2004, AJ, 127, 2544

Sheldon, E.S. et al. 2007, *e-print arXiv:0709.1153*

Siverd, R.J., Ryden, B.S., & Gaudi, B.S. 2009, *e-print arXiv:0903.2264*

Smith, D.R., Bernstein, G.M., Fischer, P., & Jarvis, R.M. 2001, ApJ, 551, 643

Tisserand, P. et al. 2007, A&A, 469, 387

Tully, R.B., & Fisher, J.R. 1977, A&A, 54, 661

Umetsu, K., Takada, M., & Broadhurst, T. 2007, Modern Physics Letters A, 22, 2099

Van Waerbeke, L., et al. 2000 A&A, 358, 30

White, S.D.M, & Frenk, C.S. 1991, ApJ, 379, 52

Wilson, G., Kaiser, N., & Luppino, G.A. 2001, ApJ 556, 601

Witman, D.M., Tyson, J., Kirkman, D., Dell'Antonia, I., Bernstein, G. 2000, Nature, 405, 143

Wyder, T.K., et al. 2007, ApJS, 173, 293

Zaritsky, D. & White, S.D.M. 1994, ApJ, 435, 599

Zetner, A.R., Kravtsov, A.V., Gnedin, O.Y. & Klypin, A.A. 2005, ApJ, 629, 219

Zheng, W. et al., 2009, ApJ, 697, 1907

Zucca, E. et al., 2006, A&A, 455, 879

Zwicky, F. 1933, Helvetica Physica Acta, 6, 110